

# Implementing contact angle boundary conditions for second-order Phase-Field models of wall-bounded multiphase flows

Ziyang Huang<sup>\*1</sup>, Guang Lin<sup>†1,2</sup>, and Arezoo M. Ardekani<sup>‡1</sup>

<sup>1</sup> *School of Mechanical Engineering, Purdue University, West Lafayette, IN 47907, USA*

<sup>2</sup> *Department of Mathematics, Purdue University, West Lafayette, IN 47907, USA*

(March 9, 2021)

## Abstract

In the present work, a general formulation is proposed to implement the contact angle boundary conditions for the second-order Phase-Field models, which is applicable to  $N$ -phase ( $N \geq 2$ ) moving contact line problems. To remedy the issue of mass change due to the contact angle boundary condition, a Lagrange multiplier is added to the original second-order Phase-Field models, which is determined by the consistent and conservative volume distribution algorithm so that the summation of the order parameters and the *consistency of reduction* are not influenced. To physically couple the proposed formulation to the hydrodynamics, especially for large-density-ratio problems, the consistent formulation is employed. The reduction-consistent conservative Allen-Cahn models are chosen as examples to illustrate the application of the proposed formulation. The numerical scheme that preserves the consistency and conservation of the proposed formulation is employed to demonstrate its effectiveness. Results produced by the proposed formulation are in good agreement with the exact and/or asymptotic solutions. The proposed method captures complex dynamics of moving contact line problems having large density ratios.

Keywords: *Contact angle; Contact line; Phase-Field; Allen-Cahn; Conservative Phase-Field; Multiphase flow*

## 1 Introduction

Moving contact line problems are ubiquitous in both natural phenomena and industrial applications. Various numerical models have been developed for this kind of problems, such as the front tracking method [58, 57, 38, 41], the level-set method [44, 50, 54, 66], the conservative level-set method [42, 43, 64, 47], and the volume-of-fluid (VOF) method [19, 48, 46, 2, 60], and the contact angle boundary conditions therein. We refer interested readers to the comprehensive review [55].

In the present study, we focus on the Phase-Field (or Diffuse-Interface) models [5], where the interface is represented as a transient layer with a small but finite thickness. Different from the sharp-interface models, which only include advection, diffusion in the Phase-Field models regularizes the singularity at the contact line. Such an additional effect can drive the contact line to move even though the no-slip boundary condition is assigned [49, 27]. One commonly used procedure to derive the contact angle boundary conditions for the Phase-Field models is in the context of wall energy relaxation [27, 45, 14, 6, 52], where the wall energy is minimized by the  $L^2$  gradient flow. Such a procedure has been extended to include surfactant [68], contact angle hysteresis [61], three fluid phases [53, 51, 67], and  $N$  ( $N \geq 2$ ) fluid phases [15]. Alternatively, the contact angle boundary conditions can also be geometry-based [13, 36, 37], where the orientation of the interface is explicitly enforced, and the one in [13] has been extended to model contact lines formed by three fluid

---

\*Email: huan1020@purdue.edu

†Email: guanglin@purdue.edu; Corresponding author

‡Email: ardekani@purdue.edu; Corresponding author

phases [65]. Most of these contact angle boundary conditions can be in general written as an inhomogeneous Neumann boundary condition. Among various Phase-Field models, the Cahn-Hilliard Phase-Field model [9] is most popularly used to model moving contact line problems, since the contact angle boundary conditions can be directly applied without influencing the mass conservation. The Cahn-Hilliard model is a 4th-order partial differential equation (PDE) and therefore we also call it a 4th-order Phase-Field model here. To uniquely solve it, each boundary requires two boundary conditions, one of which is determined by mass conservation. Flexibility is given to the remaining one to control the morphology of the interface, which is achieved by implementing the contact angle boundary conditions. The popularity of implementing the Cahn-Hilliard model has motivated several theoretical analyses, e.g., in [27, 45, 63, 62, 59], and comparison studies, e.g., in [13, 34].

More recently, the second-order Phase-Field models, such as the conservative Phase-Field models [11, 39] and the conservative Allen-Cahn models [8, 24], have attracted lots of attention and became popular in modeling both two-phase flows, e.g., in [11, 40, 28, 31, 30, 23], and  $N$ -phase ( $N \geq 2$ ) flows, e.g., in [3, 21, 24]. They are modified from the Allen-Cahn model [4] and enjoy several desirable properties that the Cahn-Hilliard model does not have, but are important in multiphase flow modeling, such as conserving volume enclosed by the interface, preserving under-resolved structures, and the maximum principle [8, 33, 35, 32, 10, 39, 23, 24]. Moreover, it is easier and more efficient to solve the 2nd-order model than the 4th-order one. However, difficulty appears when these 2nd-order Phase-Field models are used to model problems including moving contact lines, because only a single boundary condition is needed. This boundary condition is always determined by the mass conservation and the homogeneous Neumann boundary condition is normally required. Consequently, only  $90^\circ$  contact angle can be assigned at the wall boundary, which strongly restricts the application of the second-order Phase-Field models. So far, the second-order Phase-Field models have not been able to share the fruitful progress made in the implementation of the contact angle boundary conditions for moving contact line problems.

The present study attempts to address this issue and proposes a novel and general formulation which has the following desirable properties:

- It is valid for both two-phase and  $N$ -phase ( $N > 2$ ) cases.
- It does not rely on the specific forms of the 2nd-order Phase-Field models and the contact angle boundary conditions.
- It grants the *consistency of reduction*, the mass conservation of each phase, and the summation of the volume fractions to be unity.
- It incorporates the *consistency of mass conservation* and the *consistency of mass and momentum transport* for large-density-ratio problems.

The idea is to introduce a Lagrange multiplier to the original Phase-Field model, so that the mass change due to the contact angle boundary condition is compensated. The Lagrange multiplier needs to be carefully designed to avoid producing voids, overfilling, or fictitious phases, and therefore the consistent and conservative volume distribution algorithm is employed [24]. Finally, the coupling to the hydrodynamics is accomplished by using the consistent formulation [23], which is essential for large-density-ratio problems. This general formulation is applied to the reduction-consistent conservative Allen-Cahn models [7, 24], and various tests are performed to demonstrate its effectiveness.

The rest of the paper is organized as follows. In Section 2, the general formulation to include the contact angle boundary condition in the second-order Phase-Field models and its coupling to the hydrodynamics are elaborated, followed by its application to the conservative Allen-Cahn models. In Section 3, the numerical methods to solve the complete system is briefly summarized. In Section 4, various numerical tests are performed to demonstrate the proposed formulation in moving contact line problems. In Section 5, the present study is concluded and some possible future directions are introduced.

## 2 Definitions and governing equations

We first define the problem in Section 2.1. Then, the general formulation of implementing the contact angle boundary condition for a second-order Phase-Field model is proposed and elaborated in Section 2.2.1,

along with its coupling to the hydrodynamics in Sections 2.2.2 and 2.2.3. Finally, two specific examples, one for two-phase problems and the other for  $N$ -phase problems, are provided in Section 2.3, which are the applications of the proposed general formulation described in Section 2.2.1 to the conservative Allen-Cahn models.

## 2.1 Basic definitions

There are  $N$  ( $N \geq 2$ ) different incompressible and immiscible fluid phases inside domain  $\Omega$ , and their locations are labeled by a set of order parameters  $\{\phi_p\}_{p=1}^N$ . The order parameters need to follow the summation constraint:

$$\sum_{p=1}^N C_p = \sum_{p=1}^N \frac{1 + \phi_p}{2} = 1 \quad \text{or} \quad \sum_{p=1}^N \phi_p = 2 - N, \quad (1)$$

where  $\{C_p\}_{p=1}^N$  are the volume fractions of the phases and therefore their summation is always unity. In other words, void or overfilling is not allowed to appear. The densities and viscosities of the phases are denoted by  $\{\rho_p\}_{p=1}^N$  and  $\{\mu_p\}_{p=1}^N$ , respectively. As a result, the mixture density and viscosity are

$$\rho = \sum_{p=1}^N \rho_p \frac{1 + \phi_p}{2}, \quad \mu = \sum_{p=1}^N \mu_p \frac{1 + \phi_p}{2}. \quad (2)$$

Each pair of phases has a surface tension, for example,  $\sigma_{p,q}$  denotes the surface tension at the interface of Phases  $p$  and  $q$ .  $\theta_{p,q}$  is the contact angle in between Phase  $p$  and a wall boundary and formed by Phases  $p$  and  $q$ . Notice that  $\sigma_{p,q}$  ( $= \sigma_{q,p}$ ) is symmetry, while  $\theta_{p,q}$  and  $\theta_{q,p}$  are supplementary angles, i.e.,  $\theta_{p,q} + \theta_{q,p} = \pi$ ,  $1 \leq p, q \leq N$ . The flow velocity is the volume-averaged velocity of the phases and its divergence is:

$$\nabla \cdot \mathbf{u} = 0, \quad (3)$$

since each phase is incompressible [1, 16, 22]. If there are only two phases, we denote  $\phi_1 = \phi$ ,  $\phi_2 = -\phi$ ,  $\sigma = \sigma_{1,2}$ , and  $\theta = \theta_{1,2}$  for convenience. Consequently, one only needs to solve  $\phi_1$  (or  $\phi$ ), and  $\phi_2$  is obtained automatically from Eq.(1), or equivalently  $\phi_2 = -\phi_1 = -\phi$ . Unless otherwise specified, the domain boundary  $\partial\Omega$  is composed of wall boundaries, although periodic, inflow, or outflow boundaries can be incorporated, depending on specific problems.

## 2.2 Governing equations

Here, the emphasis is on answering how to implement the contact angle boundary condition in the second-order Phase-Field model with the proposed general formulation. The hydrodynamics is included, following the *consistency of mass conservation* and the *consistency of mass and momentum transport* [25, 23].

### 2.2.1 The proposed general formulation

The general form of the second-order Phase-Field model can be written as

$$\frac{\partial \phi_p}{\partial t} + \nabla \cdot (\mathbf{u} \phi_p) = \mathcal{L}_p[\{\phi_q\}_{q=1}^N] \quad \text{in } \Omega, \quad 1 \leq p \leq N, \quad (4)$$

where  $\mathcal{L}$  represents a functional of the order parameters, and the highest (spatial) derivatives included are the second-order derivatives. This is the reason that Eq.(4) is called the second-order Phase-Field model. Because of the divergence-free velocity Eq.(3), the convection term in Eq.(4) has been written in a conservative form. To be physically admissible,  $\mathcal{L}$  has the following properties:

$$\sum_{q=1}^N \mathcal{L}_q = 0, \quad \int_{\Omega} \mathcal{L}_p d\Omega = 0 \quad \text{with} \quad \mathbf{n} \cdot \nabla \phi_p = 0 \quad \text{at} \quad \partial\Omega, \quad \mathcal{L}_p|_{\phi_p=-1} = 0, \quad 1 \leq p \leq N. \quad (5)$$

The first property in Eq.(5) comes from the summation of the order parameters Eq.(1). The second one implies the mass conservation of Phase  $p$ , which is shown more clearly after Eq.(4) is integrated over  $\Omega$ :

$$\frac{d}{dt} \int_{\Omega} \phi_p d\Omega + \int_{\partial\Omega} \mathbf{n} \cdot \mathbf{u} \phi_p d\Gamma = 0, \quad 1 \leq p \leq N. \quad (6)$$

To achieve the mass conservation of individual phases, i.e., Eq.(6), usually relies on the homogeneous Neumann boundary condition which therefore is included in the second property of  $\mathcal{L}$  in Eq.(5). The last property in Eq.(5) corresponds to the *consistency of reduction* in the sense that Phase  $p$  will not be produced if it is absent, i.e.,  $(\partial\phi_p/\partial t)|_{\phi_p=-1} = 0$ . However, in the present study, the contact angle boundary condition, i.e.,

$$\mathbf{n} \cdot \nabla \phi_p = \mathcal{F}_p^w [\{\phi_q\}_{q=1}^N; \{\theta_{q,r}\}_{q,r=1}^N] \quad \text{at} \quad \partial\Omega, \quad 1 \leq p \leq N, \quad (7)$$

needs to be implemented instead of the homogeneous Neumann boundary condition. As a result, the second property of  $\mathcal{L}$  in Eq.(5) is not guaranteed, and the mass conservation of each phase, i.e., Eq.(6), is probably violated. It should be noted that the notation in Eq.(7) is simplified, and  $\mathcal{F}^w$  and  $\{\theta_{p,q}\}_{p,q=1}^N$  can be different at individual wall boundaries in practice. Similar to  $\mathcal{L}$ , physically admissible  $\mathcal{F}^w$  has the following properties:

$$\sum_{q=1}^N \mathcal{F}_q^w = 0, \quad \mathcal{F}_p^w|_{\phi_p=-1} = 0, \quad 1 \leq p \leq N, \quad (8)$$

compatible with the summation of the order parameters Eq.(1) and the *consistency of reduction*, respectively.

In order to implement the contact angle boundary condition Eq.(7), while other physical principles are not violated, we propose to modify the second-order Phase-Field model Eq.(4) to be

$$\frac{\partial\phi_p}{\partial t} + \nabla \cdot (\mathbf{u}\phi_p) = \mathcal{L}_p[\{\phi_q\}_{q=1}^N] + L_p^w \quad \text{in} \quad \Omega, \quad 1 \leq p \leq N, \quad (9)$$

where  $L^w$  is the newly introduced Lagrange multiplier and has the following properties:

$$\sum_{q=1}^N L_q^w = 0, \quad \int_{\Omega} L_p^w d\Omega = - \int_{\Omega} \mathcal{L}_p d\Omega = S_p \quad \text{with} \quad \mathbf{n} \cdot \nabla \phi_p = \mathcal{F}_p^w \quad \text{at} \quad \partial\Omega, \quad L_p^w|_{\phi_p=-1} = 0, \quad (10)$$

$$1 \leq p \leq N,$$

to satisfy the summation of the order parameters Eq.(1), mass conservation of the phases Eq.(6), and *consistency of reduction*, as explained below Eq.(5). Now, the question turns into determining  $L^w$  that satisfies Eq.(10). This question is successfully addressed by the consistent and conservative volume distribution algorithm in [24]. Specifically,  $L^w$  is determined by

$$L_p^w = \sum_{q=1}^N W_{p,q} B_q^w, \quad 1 \leq p \leq N, \quad (11)$$

$$\sum_{q=1}^N \left( \int_{\Omega} W_{p,q} d\Omega \right) B_q^w = S_p, \quad W_{p,q} = \begin{cases} -(1 + \phi_p)(1 + \phi_q), & p \neq q, \\ (1 + \phi_p)(1 - \phi_q), & p = q. \end{cases}$$

Notice that  $B^w$  is solved from a  $N$ -by- $N$  symmetry and diagonally dominant linear system. More details and analyses of the volume distribution algorithm are provided in [24] and one can easily show that the conditions in Eq.(10) are all satisfied by  $L^w$  in Eq.(11).

When there are only two phases, as shown in [24], one can obtain  $L^w$  from Eq.(11) explicitly, i.e.,

$$L_p^w = \frac{W_p}{\int_{\Omega} W_p d\Omega} S_p, \quad W_p = 1 - \phi_p^2, \quad p = 1, 2. \quad (12)$$

As a result, we have the following two-phase second-order Phase-Field model with the contact angle boundary condition:

$$\frac{\partial\phi}{\partial t} + \nabla \cdot (\mathbf{u}\phi) = \mathcal{L}[\phi] + L^w \quad \text{in} \quad \Omega, \quad \mathbf{n} \cdot \nabla \phi = \mathcal{F}^w[\phi; \theta] \quad \text{at} \quad \partial\Omega, \quad (13)$$

$$L^w = \frac{W}{\int_{\Omega} W d\Omega} S, \quad S = - \int_{\Omega} \mathcal{L} d\Omega, \quad W = 1 - \phi^2.$$

The proposed general formulation is summarized as follows: given any physically admissible second-order Phase-Field model, i.e., Eq.(4) satisfying Eq.(5), and contact angle boundary condition, i.e., Eq.(7) satisfying Eq.(8), a new second-order Phase-Field model is developed, i.e., Eq.(9) and Eq.(11), with the same contact angle boundary condition Eq.(7), so that the summation of the order parameters Eq.(1), mass conservation of the phases Eq.(6), and *consistency of reduction* are all satisfied. For two-phase problems, the proposed formulation becomes Eq.(13).

### 2.2.2 Mass conservation and consistent formulation

Before coupling to the hydrodynamics, we need to first determine the actual mass transport governed by the newly developed second-order Phase-Field model Eq.(9) and the mixture density Eq.(2). For a clear presentation, we combine  $\mathcal{L}$  and  $L^w$ , i.e.,  $L = \mathcal{L} + L^w$ , in Eq.(9), and obtain

$$\frac{\partial \phi_p}{\partial t} + \nabla \cdot (\mathbf{u} \phi_p) = L_p \quad \text{in } \Omega, \quad 1 \leq p \leq N, \quad (14)$$

$$\int_{\Omega} L_p d\Omega = 0, \quad 1 \leq p \leq N, \quad (15)$$

with the contact angle boundary condition Eq.(7). Next, we apply the consistent formulation [23]:

$$\nabla \cdot (W_Q(\phi_p) \nabla Q_p) = L_p \quad \text{in } \Omega, \quad \mathbf{n} \cdot \nabla Q_p = 0 \quad \text{at } \partial\Omega, \quad W_Q(\phi) = 1 - \phi^2, \quad 1 \leq p \leq N. \quad (16)$$

The consistent formulation Eq.(16) relates the non-local term  $L$  to a local conservative form. Notice that the homogeneous Neumann boundary condition of  $Q$  is obtained from Eq.(15). After considering Eq.(14) and Eq.(16), the newly proposed Phase-Field model Eq.(9) is equivalent to

$$\frac{\partial \phi_p}{\partial t} + \nabla \cdot \mathbf{m}_{\phi_p} = 0, \quad (17)$$

where the Phase-Field flux  $\mathbf{m}_{\phi}$  is

$$\mathbf{m}_{\phi_p} = \mathbf{u} \phi_p - W_Q(\phi_p) \nabla Q_p, \quad 1 \leq p \leq N. \quad (18)$$

Following the formulation in [22], we can immediately obtain the consistent mass flux:

$$\mathbf{m} = \sum_{p=1}^N \frac{\rho_p}{2} (\mathbf{u} + \mathbf{m}_{\phi_p}), \quad (19)$$

which leads to the mass conservation equation:

$$\frac{\partial \rho}{\partial t} + \nabla \cdot \mathbf{m} = 0, \quad (20)$$

after the mixture density Eq.(2) is included. The derivations in this section is based on the *consistency of mass conservation* proposed and analyzed in [25, 22, 23].

### 2.2.3 Momentum equation

The fluid motion is governed by the momentum equation:

$$\frac{\partial(\rho \mathbf{u})}{\partial t} + \nabla \cdot (\mathbf{m} \otimes \mathbf{u}) = -\nabla P + \nabla \cdot [\mu(\nabla \mathbf{u} + \nabla \mathbf{u}^T)] + \rho \mathbf{g} + \mathbf{f}_s, \quad (21)$$

where  $P$  is the pressure,  $\mathbf{g}$  is the gravity, and  $\mathbf{f}_s$  is the surface tension force. Notice that the same mass flux  $\mathbf{m}$ , defined in Eq.(19), appears in both the mass conservation equation Eq.(20) and the inertial term of the momentum Eq.(21), which is required by the *consistency of mass and momentum transport* [25, 23]. As a result, the momentum equation Eq.(21) satisfies not only the momentum conservation but also kinetic

energy conservation (neglecting the viscosity, gravity and surface tension) and Galilean invariance, see [22]. It should also be noted that simply using  $\nabla \cdot (\rho \mathbf{u} \otimes \mathbf{u})$  as the nonlinear inertial term in the momentum equation cannot simultaneously achieve these physical properties .

In the present study, the surface tension force is

$$\mathbf{f}_s = \xi \nabla \phi, \quad \xi = \lambda \left( \frac{1}{\eta^2} g'(\phi) - \nabla^2 \phi \right), \quad \lambda = \frac{3}{2\sqrt{2}} \sigma \eta, \quad g(\phi) = \frac{1}{4} (1 - \phi^2)^2, \quad (22)$$

for two-phase problems, and

$$\mathbf{f}_s = \frac{1}{2} \sum_{p=1}^N \xi_p \nabla \phi_p, \quad \xi_p = \sum_{q=1}^N \lambda_{p,q} \left[ \frac{1}{\eta^2} (g'_1(\phi_p) - g'_2(\phi_p + \phi_q)) + \nabla^2 \phi_q \right], \quad (23)$$

$$\lambda_{p,q} = \frac{3}{2\sqrt{2}} \sigma_{p,q} \eta, \quad g_1(\phi) = \frac{1}{4} (1 - \phi^2)^2, \quad g_2(\phi) = \frac{1}{4} \phi^2 (\phi + 2)^2,$$

for multiphase problems. Here,  $\lambda$  or  $\lambda_{p,q}$  is the mixing energy density,  $\eta$  is the interface thickness,  $g(\phi)$ ,  $g_1(\phi)$ , and  $g_2(\phi)$  are potential functions, and  $g'(\phi)$ ,  $g'_1(\phi)$ , and  $g'_2(\phi)$  are their derivatives with respect to  $\phi$ . Eq.(22) and Eq.(23) have been widely used in two-phase and  $N$ -phase flows, e.g., in [26, 17, 25, 23, 16, 22, 20, 21].

## 2.3 Application to the conservative Allen-Cahn models

In the present study, the conservative Allen-Cahn models are considered as examples to demonstrate the effectiveness of the general formulation developed in Section 2.2.1. Specific formulations of  $\mathcal{L}$  in the second-order Phase-Field model Eq.(4) and  $\mathcal{F}^w$  in the contact angle boundary condition Eq.(7) are provided, and both two-phase and  $N$ -phase formulations are considered.

### 2.3.1 Two-Phase model

The two-phase conservative Allen-Cahn model proposed in [8] is considered, where  $\mathcal{L}$  in the model is defined as

$$\mathcal{L}[\phi] = M \lambda \left( \nabla^2 \phi - \frac{1}{\eta^2} g'(\phi) \right) + L^c, \quad (24)$$

$$L^c = W B^c, \quad W = 1 - \phi^2, \quad B^c = \frac{\int_{\Omega} \frac{M \lambda}{\eta^2} g'(\phi) d\Omega}{\int_{\Omega} W d\Omega}.$$

Here,  $M$  is the mobility. One can easily show that  $\mathcal{L}$  in Eq.(24) satisfies all the conditions in Eq.(5), and therefore it is physically admissible. The two-phase contact angle boundary condition considered is

$$\mathcal{F}^w[\phi; \theta] = \frac{\sqrt{2}}{3\eta} \cos(\theta) g'_w(\phi), \quad (25)$$

which is proposed in [27] from a wall functional. Here,  $g_w(\phi)$  is an interpolation function satisfying  $g_w(\pm 1) = \pm 1$  and  $g'_w(\pm 1) = 0$ , and we choose  $g_w(\phi) = \sin\left(\frac{\pi}{2}\phi\right)$ , like [51, 6, 25, 52]. Another choice of  $g_w(\phi)$  is the Hermite polynomial, i.e.,  $g_w(\phi) = \frac{1}{2}\phi(3 - \phi^2)$ , used, e.g., in [27, 14, 67, 61]. Our tests do not find distinguishable difference of these two choices. Again,  $\mathcal{F}^w$  in Eq.(25) is physically admissible since it satisfies Eq.(8).

Then, we apply the proposed formulations in Section 2.2.1, i.e., Eq.(13), which introduces  $L^w$  to the two-phase conservative Allen-Cahn model. Since both  $L^c$  in Eq.(24) and  $L^w$  in Eq.(13) share an identical weight function  $W = 1 - \phi^2$ , we can combine  $L^c$  and  $L^w$ , i.e.,  $L^a = L^c + L^w$ , as well as  $B^c$  and  $B^w$ , i.e.,  $B = B^c + B^w$ , for simplicity. As a result, we reach the following system:

$$\frac{\partial \phi}{\partial t} + \nabla \cdot (\mathbf{u} \phi) = M \lambda \left( \nabla^2 \phi - \frac{1}{\eta^2} g'(\phi) \right) + L^a \quad \text{in } \Omega, \quad \mathbf{n} \cdot \nabla \phi = \frac{\sqrt{2}}{3\eta} \cos(\theta) g'_w(\phi) \quad \text{at } \partial\Omega, \quad (26)$$

$$L^a = W B, \quad W = 1 - \phi^2, \quad B = \frac{\int_{\Omega} M \lambda \left( \frac{1}{\eta^2} g'(\phi) - \nabla^2 \phi \right) d\Omega}{\int_{\Omega} W d\Omega}, \quad g_w(\phi) = \sin\left(\frac{\pi}{2}\phi\right).$$

One can understand  $L^a$  in Eq.(26) serving as a Lagrange multiplier to compensate the mass change inside  $\Omega$  from  $\frac{M\lambda}{\eta^2}g'(\phi)$  and at  $\partial\Omega$  from the contact angle boundary condition.

### 2.3.2 $N$ -Phase model

Here, we consider the reduction-consistent multiphase conservative Allen-Cahn model proposed in [24], where  $\mathcal{L}$  is defined as

$$\begin{aligned} \mathcal{L}_p[\{\phi_q\}_{q=1}^N] &= M\lambda_0 \left( \nabla^2 \phi_p - \frac{1}{\eta^2} \left( g'(\phi_p) - \frac{1+\phi_p}{2} L^s \right) \right) + L_p^c, \quad 1 \leq p \leq N, \\ L^s &= \sum_{q=1}^N g'(\phi_q), \quad L_p^c = \sum_{q=1}^N W_{p,q} B_q^c, \quad \int_{\Omega} L_p^c d\Omega = \int_{\Omega} \frac{M\lambda_0}{\eta^2} \left( g'(\phi_p) - \frac{1+\phi_p}{2} L^s \right) d\Omega. \end{aligned} \quad (27)$$

Here,  $\lambda_0 = \max(\lambda_{p,q})$ , and  $L^c$  is also determined from the consistent and conservative volume distribution algorithm [24]. Therefore  $\mathcal{L}$  in Eq.(27) satisfies all the conditions in Eq.(5) and is physically admissible. We employ the reduction-consistent contact angle boundary condition proposed in [15], whose formulation is

$$\begin{aligned} \mathcal{F}_p^w[\{\phi_q\}_{q=1}^N; \{\theta_{q,r}\}_{q,r=1}^N] &= \sum_{q=1}^N \zeta_{p,q} \frac{1+\phi_p}{2} \frac{1+\phi_q}{2}, \quad 1 \leq p \leq N, \\ \zeta_{p,q} &= \frac{2\sqrt{2}}{\eta} \cos(\theta_{p,q}). \end{aligned} \quad (28)$$

Notice that  $\zeta_{p,q}$  is antisymmetric, i.e.,  $\zeta_{p,q} = -\zeta_{q,p}$ . Therefore,  $\mathcal{F}^w$  in Eq.(28) also satisfies Eq.(8) and is physically admissible.

Similar to the two-phase case in Section 2.3.1, we combine  $L^c$  and  $L^w$  after applying the general formulation proposed in Section 2.2.1, i.e., Eq.(9). Therefore, we have the following system:

$$\begin{aligned} \frac{\partial \phi_p}{\partial t} + \nabla \cdot (\mathbf{u} \phi_p) &= M\lambda_0 \left( \nabla^2 \phi_p - \frac{1}{\eta^2} \left( g'(\phi_p) - \frac{1+\phi_p}{2} L^s \right) \right) + L_p^a \quad \text{in } \Omega, \\ \mathbf{n} \cdot \nabla \phi_p &= \sum_{q=1}^N \zeta_{p,q} \frac{1+\phi_p}{2} \frac{1+\phi_q}{2} \quad \text{at } \partial\Omega, \quad 1 \leq p \leq N, \\ L^s &= \sum_{q=1}^N g'(\phi_q), \quad L_p^a = \sum_{q=1}^N W_{p,q} B_q, \quad \int_{\Omega} L_p^a d\Omega = \int_{\Omega} M\lambda_0 \left( \frac{1}{\eta^2} \left( g'(\phi_p) - \frac{1+\phi_p}{2} L^s \right) - \nabla^2 \phi_p \right) d\Omega, \\ W_{p,q} &= \begin{cases} -(1+\phi_p)(1+\phi_q), & p \neq q, \\ (1+\phi_p)(1-\phi_q), & p = q. \end{cases}, \quad \zeta_{p,q} = \frac{2\sqrt{2}}{\eta} \cos(\theta_{p,q}). \end{aligned} \quad (29)$$

$L^a$  in Eq.(29) distributes the mass change due to both the Allen-Cahn model and the contact angle boundary condition consistently and conservatively, thanks to the volume distribution algorithm in [24]. Based on the analyses in [24, 15], Eq.(29) will exactly reduce to Eq.(26) with  $g_w(\phi)$  the Hermite polynomial, i.e.,  $g_w(\phi) = \frac{1}{2}\phi(3-\phi^2)$ , when there are only two phases. Then, Eq.(26) or Eq.(29) is coupled to the hydrodynamics following Section 2.2.2 and Section 2.2.3.

## 3 Discretizations

Details of applying the consistent formulation discretely and solving the momentum equation consistently and conservatively are available in our previous works [25, 23]. The balanced-force method [25, 22] is used to compute the surface tension force in Eq.(22) and Eq.(23). The (modified) conservative Allen-Cahn equations Eq.(26) and Eq.(29) are numerically solved from the 2nd-order schemes in [23, 24], where the Allen-Cahn model, i.e., the one neglecting all the Lagrange multipliers, is first solved, and then the Lagrange multipliers are obtained from satisfying the summation of the order parameters Eq.(1), the mass conservation Eq.(15), and the *consistency of reduction*. All the integrals are computed using the mid-point rule. The schemes are semi-implicit based on the 2nd-order backward difference in time. The convection terms are treated

explicitly with the 5th-order WENO scheme [29], and the diffusion terms are treated implicitly with the 2nd-order central difference [18]. The non-linear term  $g'(\phi)$  in both Eq.(26) and Eq.(29) is first linearized and then treated implicitly. More details of the schemes can be found in [23, 24].

The only difference in the present study appears at the boundary condition of the order parameters, where the homogeneous Neumann boundary condition is replaced by the contact angle boundary condition. This requires only minor changes, and the contact angle boundary condition is implemented explicitly following [25, 22, 14, 15], i.e.,

$$\mathbf{n} \cdot \nabla \phi_p^{n+1} = \mathcal{F}_p^w[\{\phi_q^{*,n+1}\}_{q=1}^N; \{\theta_{q,r}\}_{q,r=1}^N], \quad (30)$$

where  $\phi^{*,n+1}$  is an explicit evaluation of  $\phi^{n+1}$  from  $\phi^n$ ,  $\phi^{n-1}$  etc. Specifically,  $\phi^{*,n+1} = \phi^n$  for the first-order scheme and  $\phi^{*,n+1} = 2\phi^n - \phi^{n-1}$  for the second-order scheme. We use the second-order scheme in the present study.

## 4 Results

Here, we mainly focus on demonstrating the effectiveness of the proposed general formulation in Section 2.2.1, which applies to the conservative Allen-Cahn models in Section 2.3, on modeling problems including moving contact lines. The initial velocity is  $\mathbf{u} = \mathbf{0}$  and we set  $M\lambda = 10^{-3}$  and  $\eta = h$  unless otherwise specified, where  $h$  denotes the grid size.

### 4.1 Equilibrium drop

Here, we consider a semicircle liquid drop sliding on a horizontal solid wall using the two-phase model Eq.(26). The ‘‘SI’’ unit system is used here, and we skip presenting the units when we report the setup and results in this case for the sake of brevity. The water (Phase 1) has a density  $\rho_1 = 829$  and dynamic viscosity  $\mu_1 = 2.08$ , while the values of density and viscosity are  $\rho_2 = 1$  and  $\mu_2 = 0.0185$  for the air (Phase 2). The surface tension between them is  $\sigma = 37.8$ , and the gravity is pointing downward. The domain is  $[-0.5, 0.5] \times [0, 0.3]$ , and its lateral boundaries are periodic while they are no-slip walls at the top and bottom. A semicircle water drop having a radius 0.2 is initially on the middle of the bottom wall, and the air surrounds the drop. Different contact angles are assigned at the bottom wall. We use  $150 \times 45$  grid cells and time step  $\Delta t = 1 \times 10^{-4}$  to discretize the space and time, respectively.

When the gravity is neglected, i.e.,  $|\mathbf{g}| = 0$ , one can obtain the final shape of the drop exactly using the mass conservation and the contact angle [12]. The exact solution is

$$R_d = R_0 \sqrt{\frac{\pi/2}{\theta - \sin(\theta) \cos(\theta)}}, \quad H_d = R_d(1 - \cos(\theta)), \quad L_d = 2R_d \sin(\theta), \quad (31)$$

where  $R_d$ ,  $H_d$ , and  $L_d$  are the final radius, height, and spreading length of the drop, respectively,  $\theta$  is the contact angle, and  $R_0 = 0.2$  in the present case is the initial radius of the drop. Fig.1 shows the evolution of the drop with  $\theta = 60^\circ$  and  $\theta = 135^\circ$ , along with the corresponding exact final solution from Eq.(31). As expected, the drop starts with the semicircle shape, gradually approaches the final exact solution. The equilibrium shape agrees with the exact solution very well. We consider the zero contour of  $\phi$  as the interface and measure the final height and spreading length of the drop for quantitative comparison. As shown in Fig.2 a), a good agreement with the exact solution from Eq.(31) is obtained. Note that the height of the domain is changed to 0.5 for  $\theta = 135^\circ$  and  $\theta = 150^\circ$ , while the grid size remains unchanged. To investigate the convergence with respect to grid refinement, the errors of the height and spreading length of the water drop versus the grid size is shown in Fig.3, using data from  $\theta = 60^\circ$ . The observed convergence rate is close to 2nd-order.

Then, the effect of gravity is included, and the domain is changed to  $[-0.6, 0.6] \times [0, 0.24]$  without changing the grid size. Based on the asymptotic analysis for gravity-dominant cases [12], the final height of the drop becomes

$$H_d = 2 \sqrt{\frac{\sigma_{la}}{\rho_l |\mathbf{g}|}} \sin(\theta/2), \quad (32)$$



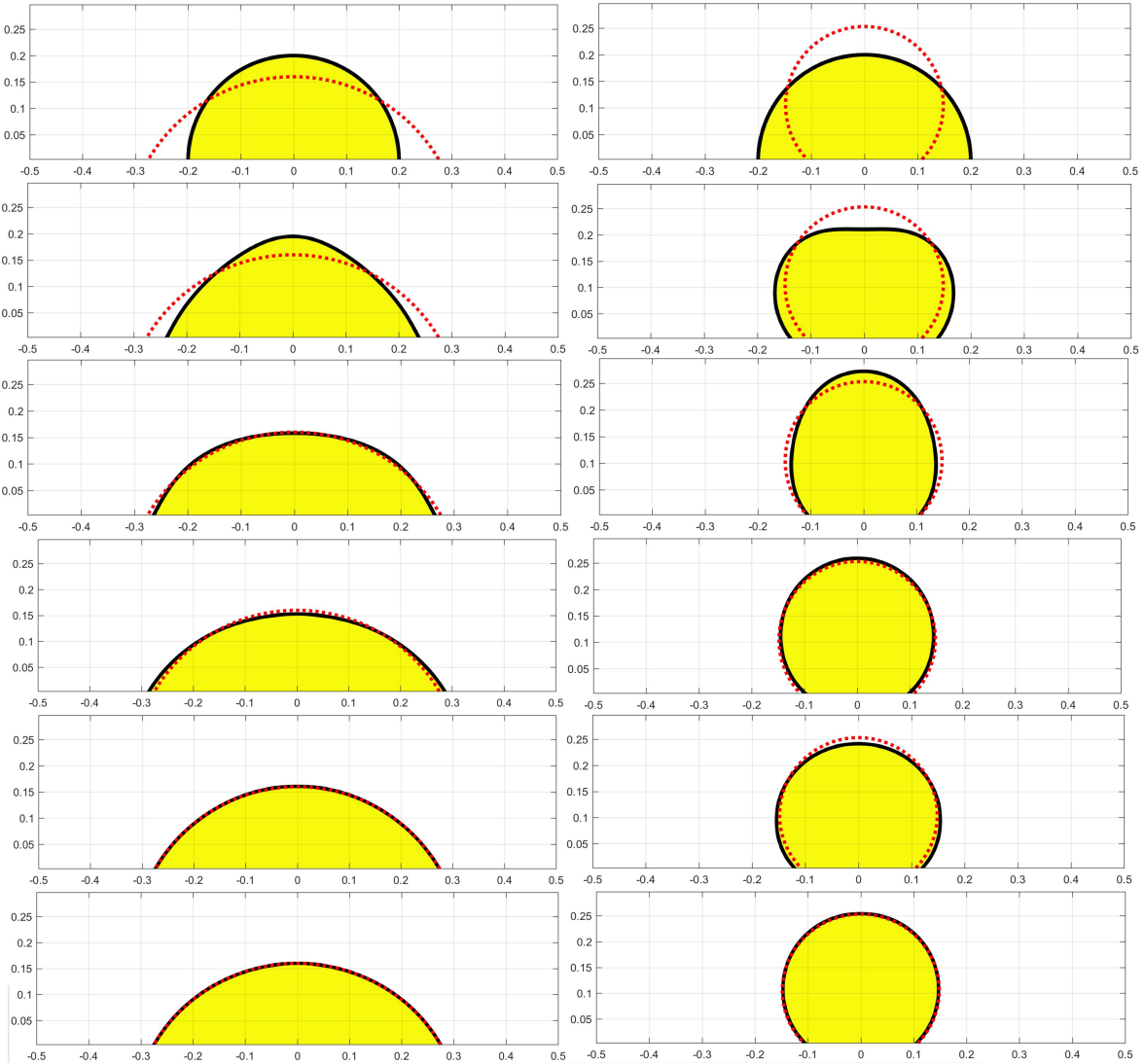


Figure 1: Evolution of the water drop using Eq.(26) with  $|\mathbf{g}| = 0$ . Yellow: water (Phase 1); White: air (Phase 2); Red dotted line: exact solution from Eq.(31). Left column:  $\theta = 60^\circ$ ; Right column:  $\theta = 135^\circ$ . From top to bottom,  $t = 0.0$ ,  $t = 0.2$ ,  $t = 0.4$ ,  $t = 1.0$ ,  $t = 1.4$ , and  $t = 2.0$  (left) and  $t = 3.0$  (right).

where  $\rho_l$ ,  $\sigma_{la}$ , and  $|\mathbf{g}|$  are the liquid density, surface tension between the liquid and air, and the magnitude of the gravity, respectively. Fig.4 shows the evolution of the drop with  $|\mathbf{g}| = 10$  and  $|\mathbf{g}| = 15$ , along with the prediction from Eq.(32). The contact angle is  $\theta = 135^\circ$ . One can observe that the drop is flattened, having a pancake-like shape, when the gravity is added. The final height of the drop matches the asymptotic prediction. Fig.2 b) shows the final height of the drop versus the gravity, and our numerical prediction overall agrees well with both the exact solution Eq.(31) without gravity and the asymptotic solution Eq.(32) with dominant gravity. Further, Fig.5 a) demonstrates the mass conservation of the proposed formulation, where the relative changes of  $\Phi$  ( $\Phi = \int_{\Omega} \phi d\Omega$ ) of the four cases reported in Fig.1 and Fig.4 are in the order of the round-off error.

Next, we supplement results of the  $N$ -phase model Eq.(29). The oil phase (Phase 3) is introduced, whose density is  $\rho_3 = 722.5$  and viscosity is  $\mu_3 = 9.5$ . The surface tensions between the oil and air and between oil and water are  $\sigma_{3,2} = 28.55$  and  $\sigma_{3,1} = 20.76$ , respectively. The domain size is  $[-1, 1] \times [0, 0.5]$  while the grid size is the same as the two-phase cases. The water drop right now is on the bottom wall with a contact angle  $\theta_{1,2} = 60^\circ$ , while the oil drop is attached to the top wall with a contact angle  $\theta_{3,2} = 120^\circ$ . Evolution of

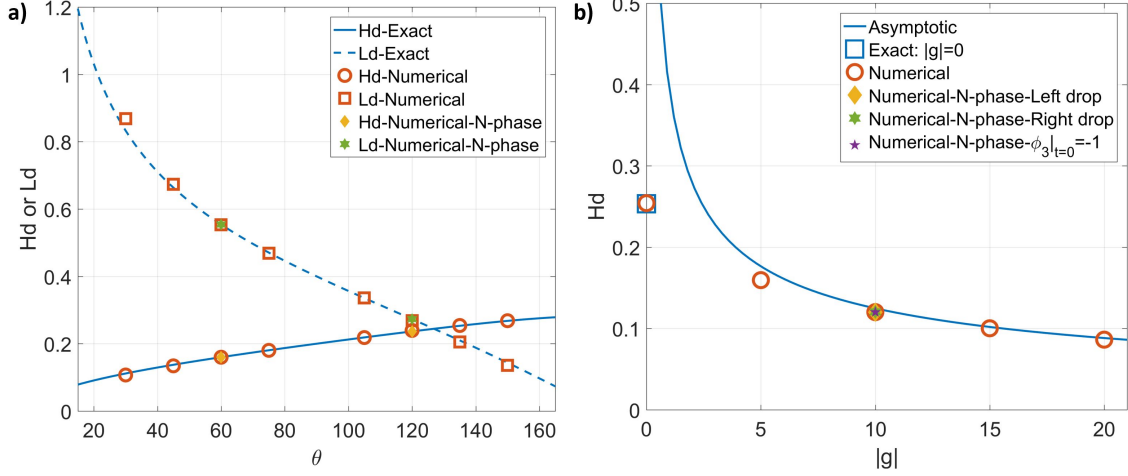


Figure 2: Height and spreading length of the drop. a)  $H_d$  and  $L_d$  versus  $\theta$  with  $|\mathbf{g}| = 0$ . b)  $H_d$  versus  $|\mathbf{g}|$  with  $\theta = 135^\circ$ .

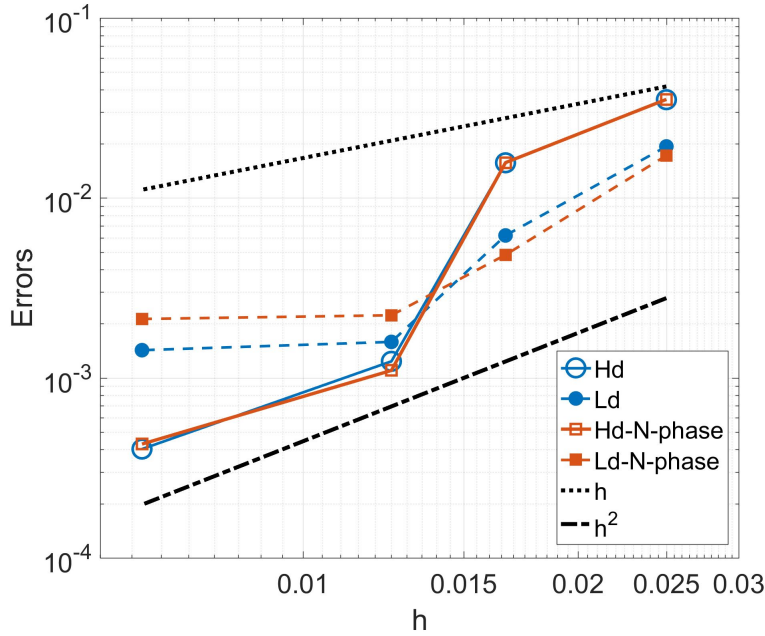


Figure 3: Errors of the height and spreading length of the water drop versus the grid size with  $\theta = \theta_{1,2} = 60^\circ$  and  $|\mathbf{g}| = 0$ .

the drops is shown in Fig.6. Not only both the water and oil drops finally match the exact solution Eq.(31) but also the shape of the water drop at different moments is indistinguishable from the two-phase solution in the left column of Fig.1. The final heights and spreading lengths of the two drops are measured and plotted in Fig.2 a) as well, and good agreement is obtained with both the exact and two-phase solutions. Fig.3 also shows the convergence behavior of the  $N$ -phase model Eq.(29), which is similar to the two-phase one Eq.(26).

Then, the gravity is added and the  $N$ -phase model Eq.(29) is again used. The surface tension between the oil and air becomes  $\sigma_{3,2} = 37.48$  so that the final heights of both the water and oil drops, predicted from the asymptotic solution Eq.(32), are the same. The domain is  $[-1, 1] \times [0, 0.3]$ , and the magnitude of the gravity is  $|\mathbf{g}| = 10$ . The contact angle of the water drop on the bottom wall is  $\theta_{1,2} = 135^\circ$ , while it is  $\theta_{3,2} = 120^\circ$  for the oil drop. Evolution of the drops are shown in Fig.7. Both of the drops are compressed

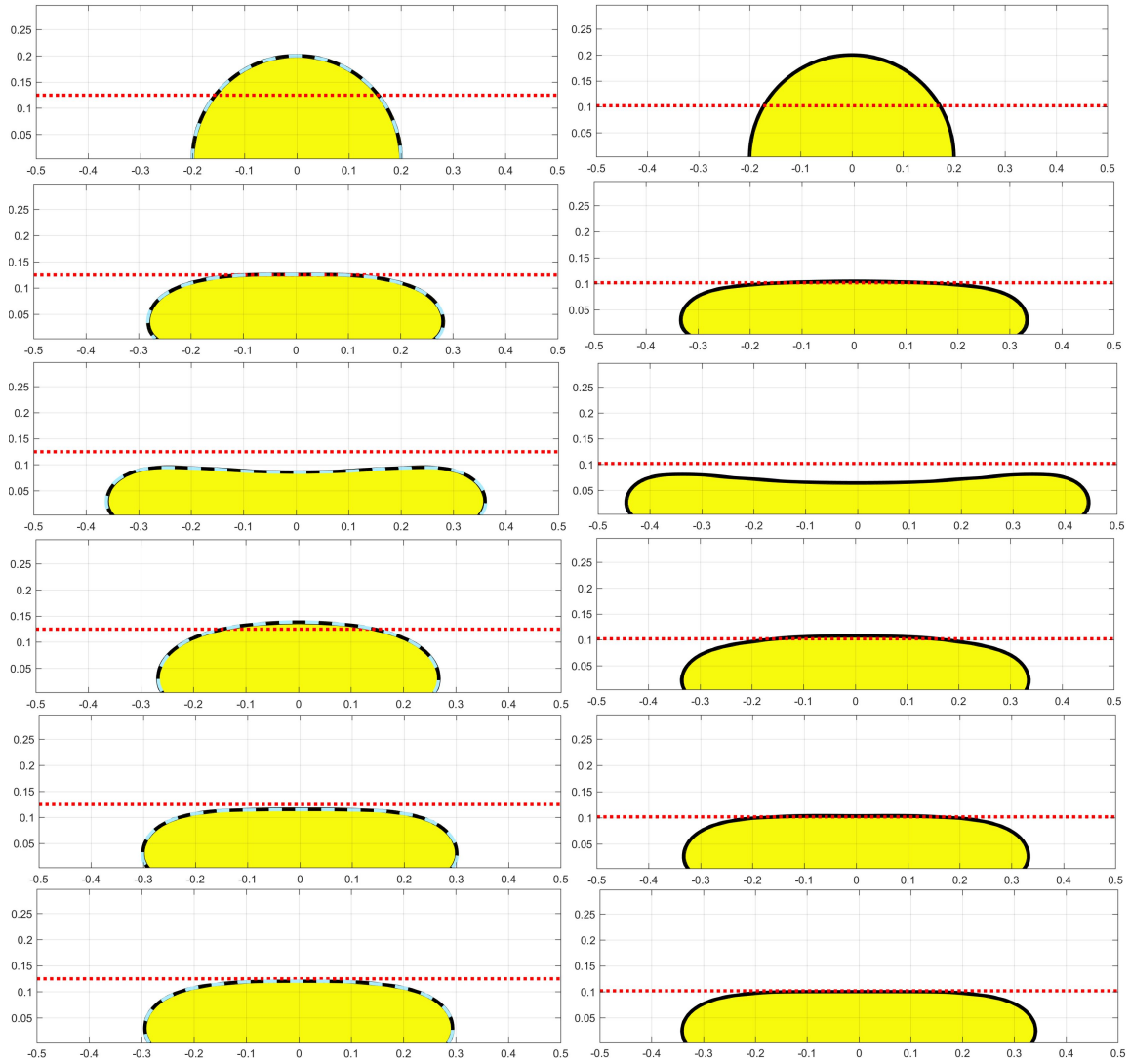


Figure 4: Evolution of the water drop using Eq.(26) with  $\theta = 135^\circ$ . Yellow: water (Phase 1); White: air (Phase 2); Red dotted line: asymptotic solution from Eq.(32); Cyan dashed line:  $N$ -phase solution from Eq.(29) with  $\phi_3|_{t=0} = -1$ . Left column:  $|\mathbf{g}| = 10$ ; Right column:  $|\mathbf{g}| = 15$ . From top to bottom,  $t = 0.0$ ,  $t = 0.2$ ,  $t = 0.4$ ,  $t = 1.0$ ,  $t = 1.4$ , and  $t = 3.0$ .

vertically and finally reach a similar height to the asymptotic prediction. Again, the water drop behaves identically to the two-phase solution in the left column of Fig.4. Fig.2 b) also includes the final heights of the two drops in this case, and they are in good agreement with both the asymptotic and two-phase solutions. We also investigate the mass conservation of the  $N$ -phase model, and the relative changes of  $\Phi_p$ , where  $p$  is the index of the phases, are in the order of the round-off error, as shown in Fig.5 b). In addition to that, the summation of the order parameters exactly satisfies Eq.(1), which is shown in Fig.5 c).

The last property the  $N$ -phase model should satisfy is the *consistency of reduction*. We repeat the  $N$ -phase case with  $|\mathbf{g}| = 10$  but only consider the left half of the domain, i.e.,  $-1 \leq x \leq 0$ . Therefore, the oil drop disappears at the beginning, i.e.,  $\phi_3|_{t=0} = -1$ . Evolution of the water drop from the  $N$ -phase model is shown in the left column of Fig.4 as well using the cyan dashed line, and the difference from the two-phase solution is negligible. This also suggests that choosing  $g_w(\phi)$  in Eq.(25) as a Sine or Hermite polynomial function has a negligible effect on the solution. Fig.8 quantitatively validates that not only the mass conservation and the summation of the order parameters are exactly satisfied by the  $N$ -phase model

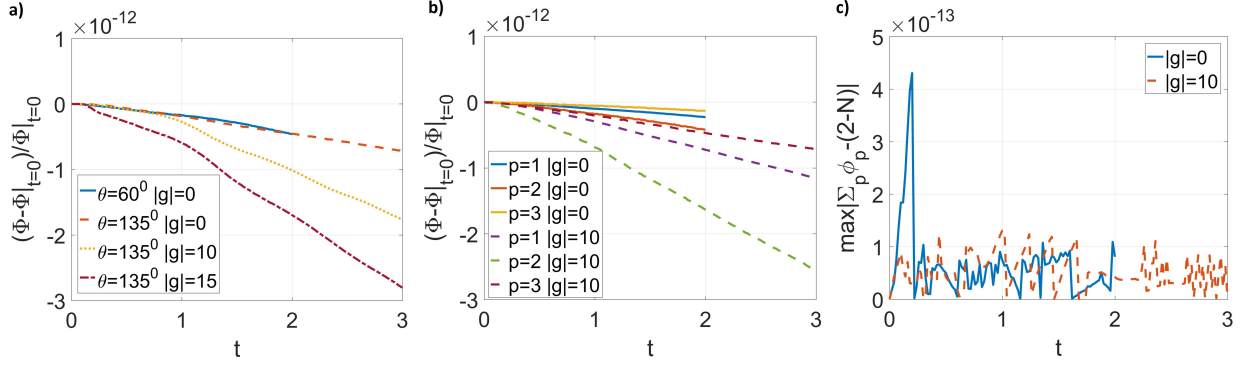


Figure 5: a) Relative changes of  $\Phi$  ( $= \int_{\Omega} \phi d\Omega$ ) from the two-phase solutions versus time. b) Relative changes of  $\Phi$  from the  $N$ -phase solutions versus time ( $p$  is the phase index). c)  $\max |\sum_p \phi_p - (2 - N)|$  from the  $N$ -phase solutions versus time.

Eq.(29) but also the *consistency of reduction* since  $\phi_3 = -1$  is true at  $\forall t > 0$ .

## 4.2 Bouncing drop

Here, we consider a falling drop bouncing back after it contacts the bottom wall, using the two-phase model Eq.(26). The density of the water (Phase 1) is  $998.207\text{kg/m}^3$  and the viscosity is  $1.002 \times 10^{-3}\text{Pa} \cdot \text{s}$ . They are  $1.2041\text{kg/m}^3$  and  $1.78 \times 10^{-5}\text{Pa} \cdot \text{s}$  for the air (Phase 2). The surface tension is  $7.28 \times 10^{-2}\text{N/m}$  and the gravity is  $\mathbf{g} = \{0, -9.8\}\text{m/s}^2$ . Non-dimensionalization is performed to the governing equations based on the density scale  $1.2041\text{kg/m}^3$ , length scale  $5 \times 10^{-3}\text{m}$ , and acceleration scale  $1\text{m/s}^2$ . The density scale is the same as the air density. The length scale is the initial height of releasing the drop, which is also the horizontal length of the domain. It is 4 times the initial radius of the drop to prevent the drop from touching the lateral sides of the domain in the investigated cases of  $\theta > 90^\circ$ . The acceleration scale is chosen for convenience so that the dimensionless value of the gravity is the same as the dimensional one. The dimensionless grid size and time step are  $h = 0.01$  and  $\Delta t = 5 \times 10^{-5}$ , respectively. The water is inside a circle having a radius 0.25 at  $(0, 1)$  in the dimensionless domain  $[-0.5, 0.5] \times [0, 1.5]$ . The boundaries are periodic at the lateral sides while no-slip at the top and bottom walls.

Fig.9 shows results with contact angle  $\theta = 165^\circ$  at the bottom wall. The drop remains circular as it is falling down. After the drop impacts on the bottom wall, it is strongly deformed to reduce the downward velocity and finally reaches a “dumbbells-like” shape. Then, the drop tries to restore the circular shape and jumps upward, leaving the bottom wall and finally arriving at a height lower than where it is initially released. This process repeats and the velocity is gradually reduced to zero. Finally, the drop settles down on the bottom wall and the equilibrium shape deviates slightly from the circular one because of the gravity.

Different contact angles at the bottom wall are considered. We observe that the drop is unable to bounce back when the contact angle is less than or equal to  $120^\circ$  and the water finally fills the bottom of the domain when the contact angle is less than or equal to  $90^\circ$ . The same behaviors are also reported in [14]. Fig.10 shows shapes of the drops from different contact angles at  $t = 0.46$ , right after the first impact to the bottom wall, and at  $t = 4.00$ . The ( $y$ -component) center of mass of the drop  $y_c$  ( $y_c = \int_{\Omega} y \frac{1+\phi}{2} d\Omega / \int_{\Omega} \frac{1+\phi}{2} d\Omega$ ) versus time is shown in Fig.11 a). Until the second impact to the bottom wall, the centers of mass from  $\theta = 165^\circ$  and  $\theta = 150^\circ$  move very similarly, as shown in Fig.11 a). However, with a smaller contact angle, length of the drop in contact with the bottom wall is larger, as shown in Fig.10. This can provide more dissipation, and as a result, the drop have a less chance to bounce back. On the other hand, each time when the drop impacts to the wall induces a large deformation of the drop, which also produces a strong dissipation due to the viscosity of the water. Therefore, from Fig.11 a), peaks of the curves describing the motion of center of mass decay very fast for the drops that bounce back, e.g., those with  $\theta = 165^\circ$  and  $150^\circ$ . For the drop that is unable to bounce back, e.g., the one with  $\theta = 120^\circ$ , it oscillates on the bottom wall, and its center of mass curve has a higher frequency but there is less attenuation between the two neighboring peaks. For the drop that will finally fill the bottom, e.g., those with  $\theta = 90^\circ$  and  $\theta = 60^\circ$ , we observe a long-term but

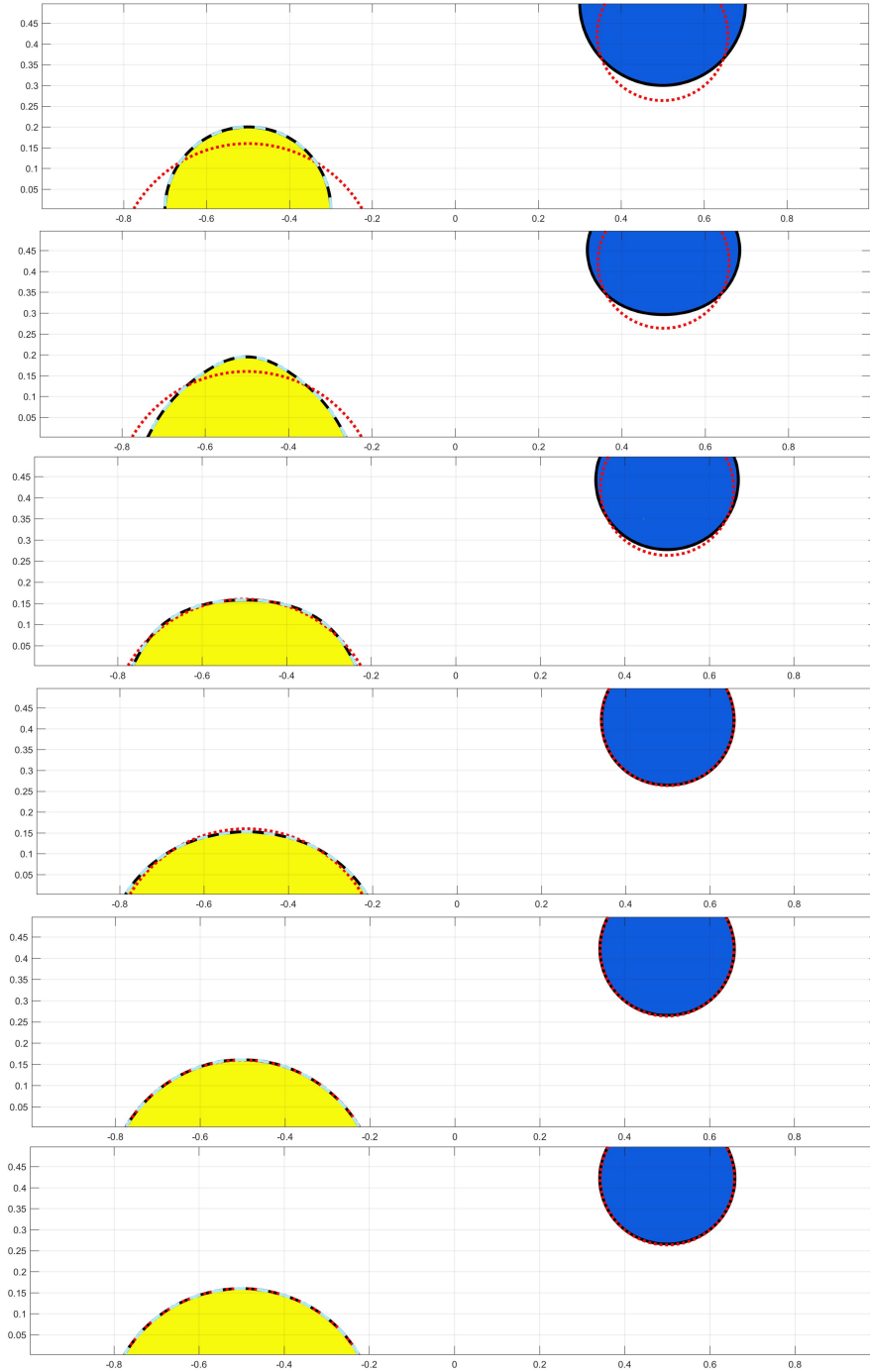


Figure 6: Evolution of the water and oil drops using Eq.(29) with  $|\mathbf{g}| = 0$ ,  $\theta_{1,2} = 60^\circ$ , and  $\theta_{3,2} = 120^\circ$ . Yellow: water (Phase 1); White: air (Phase 2); Blue: oil (Phase 3); Red dotted line: exact solution from Eq.(31); Cyan dashed line: two-phase solution from Eq.(26) in the left column of Fig.1. From top to bottom,  $t = 0.0$ ,  $t = 0.2$ ,  $t = 0.4$ ,  $t = 1.0$ ,  $t = 1.4$ , and  $t = 2.0$ .

small-amplitude oscillation of the center of mass. This is caused by the capillary wave on the horizontal water-air interface, as shown in Fig.10.

Finally, we consider the effect of the mobility  $M$ . Fig.12 shows shapes of the drops with different mobilities (or  $M\lambda$ ), and the mass centers ( $y$  component) are shown in Fig.11 b). With a larger mobility,

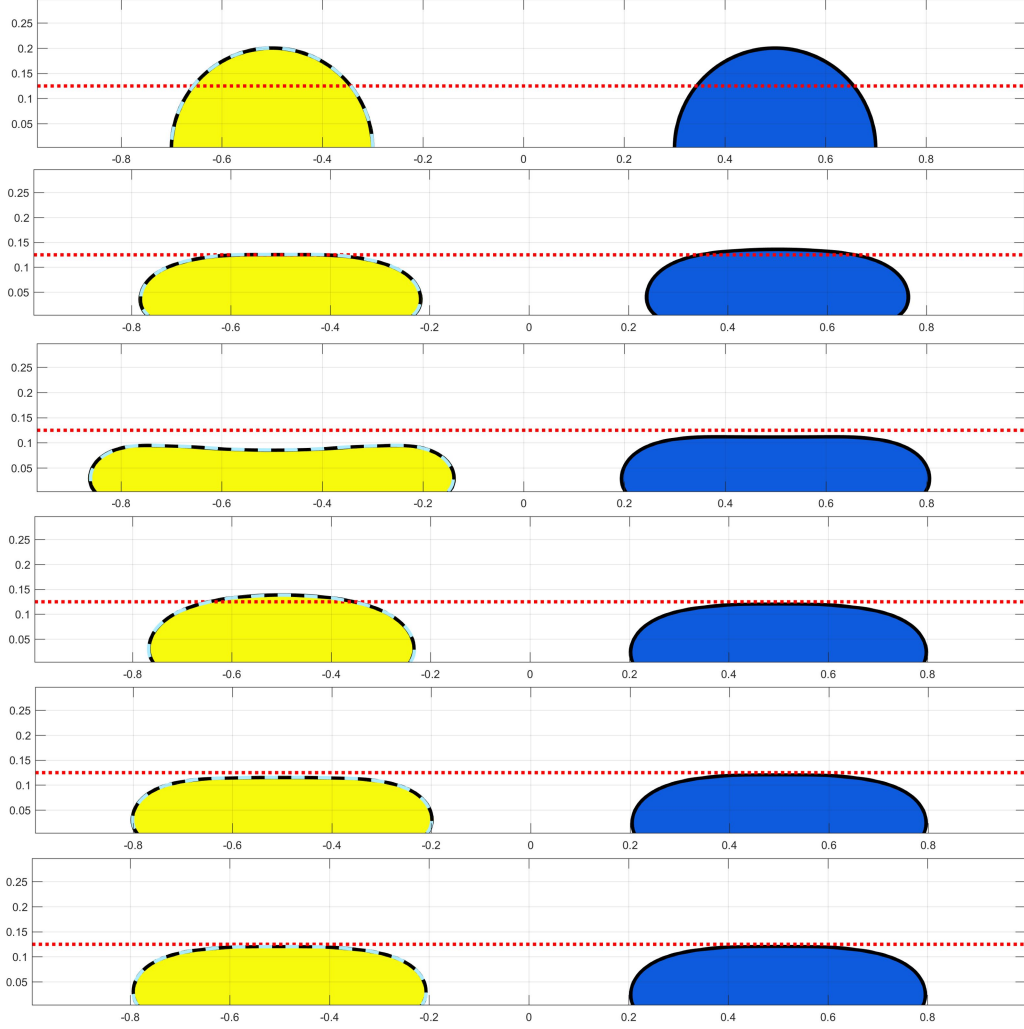


Figure 7: Evolution of the water and oil drops using Eq.(29) with  $|\mathbf{g}| = 10$ ,  $\theta_{1,2} = 135^\circ$ , and  $\theta_{3,2} = 120^\circ$ . Yellow: water (Phase 1); White: air (Phase 2); Blue: oil (Phase 3); Red dotted line: asymptotic solution from Eq.(31); Cyan dashed line: two-phase solution from Eq.(26) in the left column of Fig.4. From top to bottom,  $t = 0.0$ ,  $t = 0.2$ ,  $t = 0.4$ ,  $t = 1.0$ ,  $t = 1.4$ , and  $t = 3.0$ .

the drop becomes more “rigid” and therefore less deforms, as shown in Fig.12. On the other hand, a too “soft” drop, resulting from a small mobility, suffers from fictitious oscillation on the side close to the bottom wall. Even worse, the oscillation destroys the symmetry of the solution, and at the end produces a non-symmetry drop staying biased to left half of the domain. The drop with the smallest mobility finally is floating above the bottom wall because the interface is over-thickened. However, these unphysical behaviors are not observed in the cases with a larger mobility. As shown in Fig.11 b), there is no significant difference due to the mobility before the first impact of the drop to the bottom wall. The one with the largest mobility can only bounce back once and settles down very fast. The one with the smallest mobility bounces back multiple times although the height it returns to after the first impact is lowest among the three cases. These behaviors suggest that a larger mobility produces more dissipation.

### 4.3 Compound drops

Here, we report the compound drops sliding on a horizontal solid wall using the  $N$ -phase model Eq.(29). The material properties of the three phases are  $\rho_1 = \rho_2 = \rho_3 = 1\text{kg/m}^3$ ,  $\mu_1 = \mu_2 = 1\text{Pa} \cdot \text{s}$ ,  $\mu_3 = 1 \times 10^{-3}\text{Pa} \cdot \text{s}$ ,

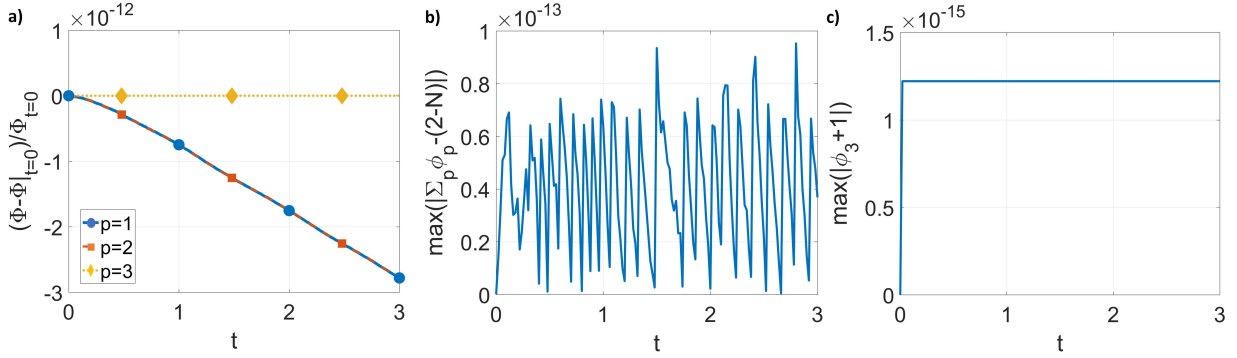


Figure 8: a) Relative changes of  $\Phi$  ( $= \int_{\Omega} \phi d\Omega$ ) from the  $N$ -phase solution versus time ( $p$  is the phase index) with  $\phi_3|_{t=0} = -1$ . b)  $\max|\sum_p \phi_p - (2 - N)|$  from the  $N$ -phase solutions versus time with  $\phi_3|_{t=0} = -1$ . c)  $\max|\phi_3 + 1|$  from the  $N$ -phase solutions versus time with  $\phi_3|_{t=0} = -1$ .

and  $\sigma_{1,2} = \sigma_{1,3} = \sigma_{2,3} = 100\text{N/m}$ , the contact angles at the bottom wall are  $\theta_{1,2} = 120^\circ$ ,  $\theta_{1,3} = 90^\circ$  and  $\theta_{2,3} = 60^\circ$ , and the gravity is neglected. The density, length, and velocity scales for non-dimensionalizing the governing equations are  $1\text{kg/m}^3$ ,  $1\text{m}$ , and  $10\text{m/s}$ , respectively. The density scale is the same as the density of Phase 1, and the length scale is the initial radius of the Phase 1 drop, denoted by  $R_{01}$ . The velocity scale, denoted by  $U$ , is determined from the inertial-capillary time scale  $T = \sqrt{\rho_1 R_{01}^3 / \sigma_{1,2}}$ , i.e.,  $U = R_{01} / T$ . As a result, the Reynolds number is  $Re = \rho_1 U R_{01} / \mu_1 = 10$  and the Weber number is  $We = \rho_1 U^2 R_{01} / \sigma_{1,2} = 1$  in this case. The dimensionless domain size is  $[-2, 2] \times [0, 1.2]$ , and the periodic and no-slip boundary conditions are assigned along the  $x$  and  $y$  axes, respectively. The space and time are discretized by  $200 \times 60$  grid cells and  $\Delta t = 1 \times 10^{-4}$ . Initially, two quarter-circular drops compound a semi-circular with a radius 1 on the middle of the bottom wall, left half of which is full of Phase 1 and the other half is Phase 2. Phase 3 occupies the remaining domain. Evolution of the drops are shown in Fig.13, along with the exact solution from [65] for the equilibrium state. The drops move towards the equilibrium shape, which agrees well with the exact solution. Quantitatively, the spreading lengths of Phases 1 and 2 are 1.0547 and 1.6871, respectively, and the relative errors are 1.614% and 1.166% after comparing to the exact ones 1.0720 and 1.7070 from [65].

Next, we investigate sliding motion of the compound drops on a translating wall. The setup is slightly changed as follows:  $\mu_2 = 0.67\text{Pa} \cdot \text{s}$ ,  $\mu_3 = 0.33 \times 10^{-3}\text{Pa} \cdot \text{s}$ , and  $\sigma_{1,2} = \sigma_{1,3} = \sigma_{2,3} = 888\text{N/m}$ . The velocity scale for non-dimensionalizing the governing equations is  $66.6\text{m/s}$ , which is the velocity of the bottom wall. As a result, the Reynolds number and Weber number become  $Re = 66.6$  and  $We = 5$ . The dimensionless height of the domain becomes 1.5, while the grid size remains the same. The bottom wall is moving backward with a unit dimensionless velocity. Results are shown in Fig.14, and the behaviors of the drops are significantly different from those on a stationary wall. We observe that the Phase 1 (yellow) drop climbs onto the Phase 2 (blue) drop, and thoroughly leave the bottom wall, sitting on the Phase 2 drop. Then, it crosses the Phase 2 drop and returns on the bottom wall. At the end, the Phase 1 drop is still in contact with the Phase 2 drop but moves in front of it.

## 5 Conclusions and future works

In the present work, we proposed a general formulation to implement the contact angle boundary conditions for the second-order Phase-Field models. The original second-order Phase-Field models are modified by adding a Lagrange multiplier that enforces the mass conservation but does not change the summation of the order parameters and the *consistency of reduction*. The newly introduced Lagrange multiplier is determined by the consistent and conservative volume distribution algorithm [24]. The proposed formulation is applicable to not only two-phase but also  $N$ -phase ( $N \geq 2$ ) cases. Then, this novel formulation is physically coupled to the hydrodynamics using the consistent formulation [23] and can be applied to large-density-ratio problems. To demonstrate its effectiveness of moving contact line simulations, we apply the proposed formulation to the reduction-consistent multiphase conservative Allen-Cahn model [24], whose two-phase version is equivalent to the one in [8]. The complete system is numerically solved by the consistent and conservative scheme

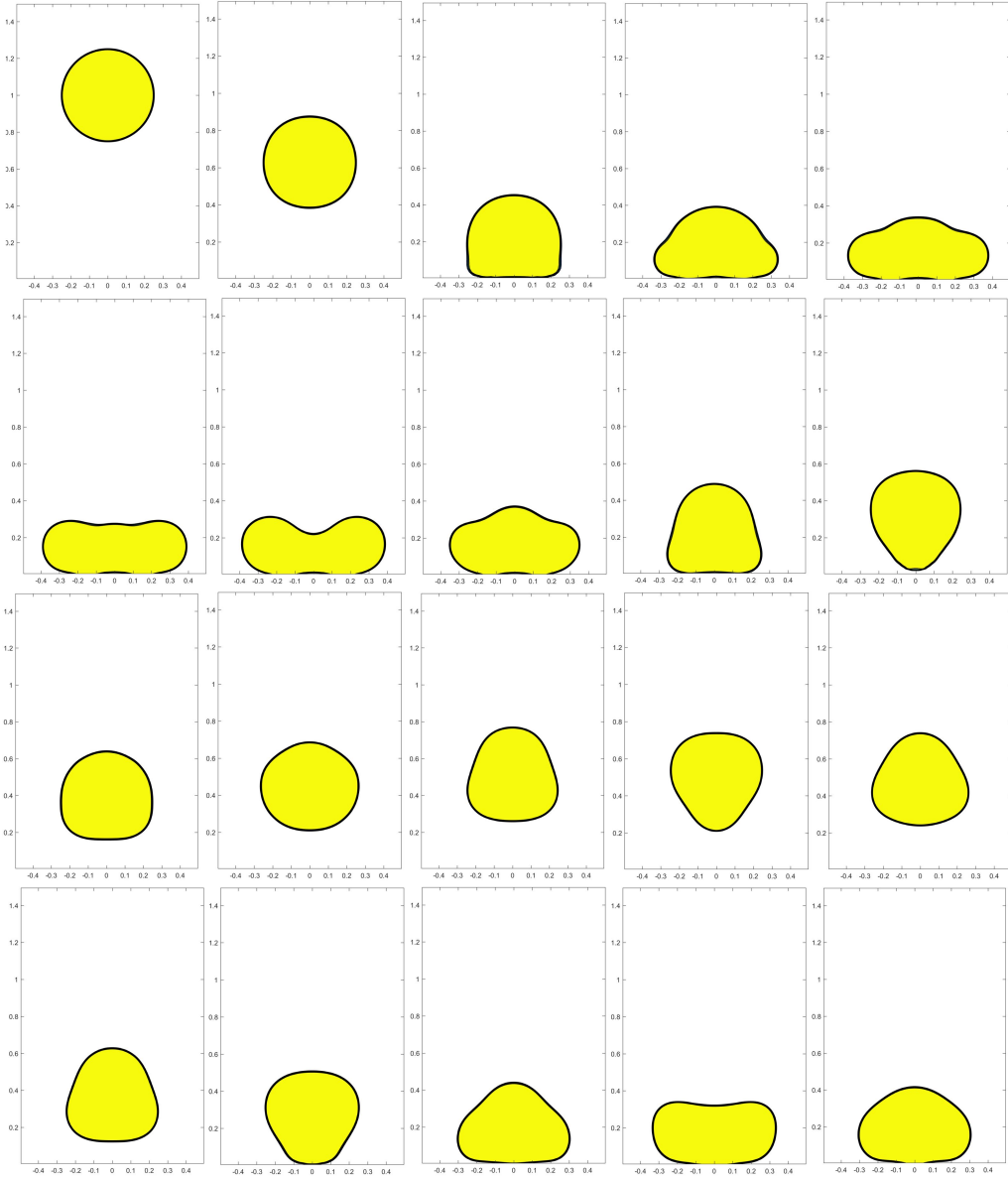


Figure 9: Results of the bouncing drop using the two-phase model Eq.(26) with  $\theta = 165^\circ$ . Yellow: water (Phase 1); White: air (Phase 2); From left to right and top to bottom:  $t = 0.00$ ,  $t = 0.30$ ,  $t = 0.44$ ,  $t = 0.46$ ,  $t = 0.48$ ,  $t = 0.50$ ,  $t = 0.52$ ,  $t = 0.56$ ,  $t = 0.60$ ,  $t = 0.64$ ,  $t = 0.68$ ,  $t = 0.72$ ,  $t = 0.80$ ,  $t = 0.85$ ,  $t = 0.90$ ,  $t = 1.00$ ,  $t = 1.05$ ,  $t = 1.10$ ,  $t = 1.15$ , and  $t = 1.20$ .

[23, 24], which preserves the mass conservation, the summation of the order parameters, and the *consistency of reduction* exactly on the discrete level, as validated in the present study. Various numerical tests are performed. The proposed formulation accurately reproduces the exact and/or asymptotic solutions for equilibrium problems, and captures important dynamical behaviors reported, e.g., in [65, 14, 15] using the Cahn-Hilliard models which are a 4th-order Phase-Field model.

The present study leaves open the possibility of using the 2nd-order Phase-Field models for moving contact line problems, which has never been considered before. Therefore, it provides plenty of new opportunities to study in the future. Generally speaking, the accuracy of the prediction heavily relies on the properties of the Phase-Field model and the contact angle boundary condition, i.e., the definitions of  $\mathcal{L}$  in Eq.(4) and  $\mathcal{F}^w$  in Eq.(7), and on the parameters therein. Since the pool of plausible Phase-Field models for moving contact



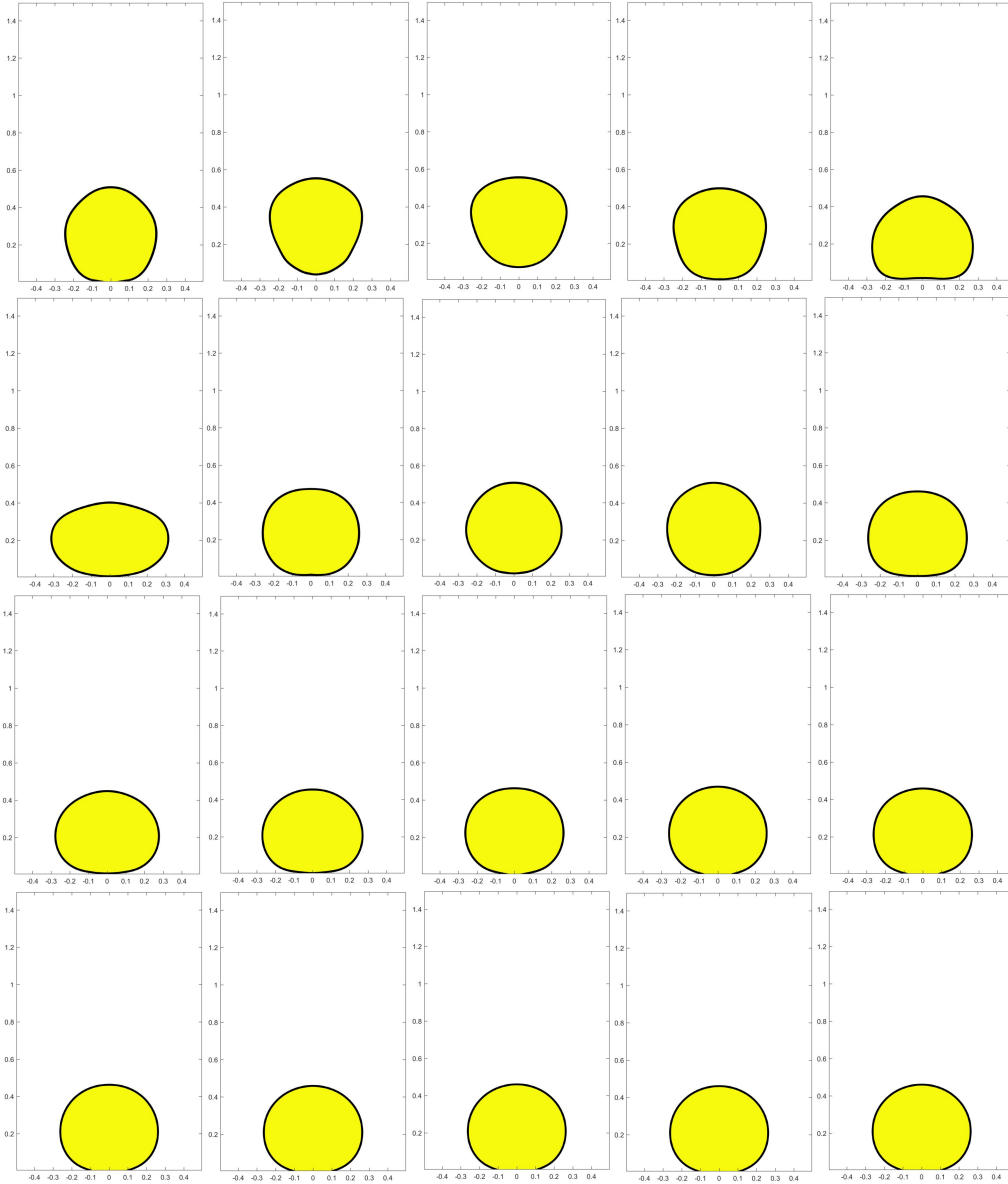


Figure 9 (continued): From left to right and top to bottom:  $t = 1.25$ ,  $t = 1.30$ ,  $t = 1.40$ ,  $t = 1.50$ ,  $t = 1.55$ ,  $t = 1.60$ ,  $t = 1.70$ ,  $t = 1.75$ ,  $t = 1.80$ ,  $t = 1.90$ ,  $t = 1.95$ ,  $t = 2.00$ ,  $t = 2.05$ ,  $t = 2.15$ ,  $t = 2.20$ ,  $t = 2.35$ ,  $t = 2.50$ ,  $t = 3.00$ ,  $t = 3.50$ , and  $t = 4.00$ .

line problems is greatly expanded, it is now not only possible but also desirable to investigate and clarify their performance. Unlike the Cahn-Hilliard models, there is little theoretical analysis of the 2nd-order Phase-Field models in moving contact line problems, e.g., the asymptotic analysis as the interface thickness tends to zero. Such an analysis is important to provide physical insights of determining the parameters in the models. We expect the present study will motivate consideration of using 2nd-order Phase-Field models in moving contact line problems as the effectiveness has been demonstrated.

## Acknowledgments

A.M. Ardekani would like to acknowledge the financial support from the National Science Foundation (CBET-1705371). This work used the Extreme Science and Engineering Discovery Environment (XSEDE) [56],

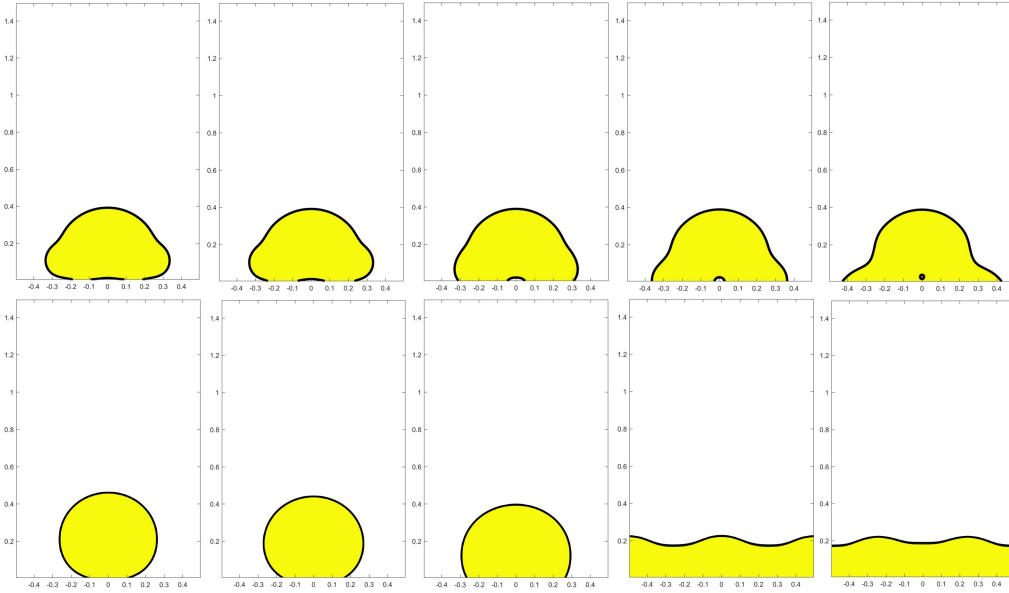


Figure 10: Shapes of the drops with different contact angles. Yellow: water (Phase 1); White: air (Phase 2); From left to right:  $\theta = 165^\circ$ ,  $\theta = 150^\circ$ ,  $\theta = 120^\circ$ ,  $\theta = 90^\circ$ , and  $\theta = 60^\circ$ . Top:  $t = 0.46$ ; Bottom:  $t = 4.00$ .

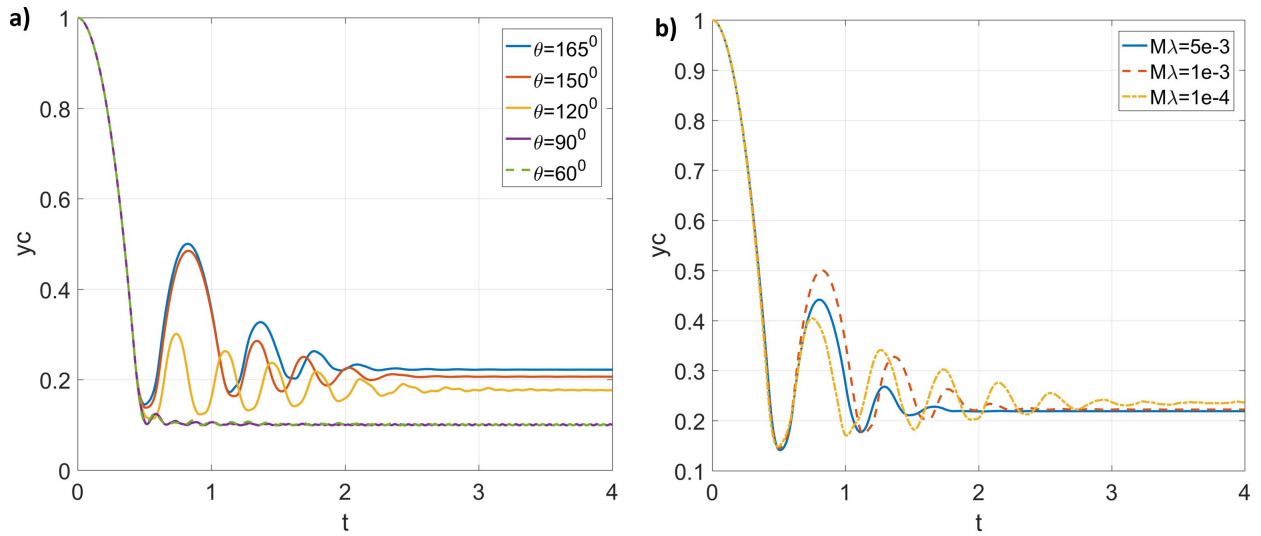


Figure 11: Mass center ( $y$  component) of the drop versus time a) with different contact angles, b) with different mobilities.

which is supported by the National Science Foundation grant number ACI-1548562 through allocation TG-CTS180066 and TG-CTS190041. G. Lin would like to acknowledge the support from National Science Foundation (DMS-1555072 and DMS-1736364, CMMI-1634832 and CMMI-1560834), and U.S. Department of Energy (DOE) Office of Science Advanced Scientific Computing Research program DE-SC0021142.

## References

- [1] H. Abels, H. Garcke, and G. Grun. Thermodynamically consistent, frame indifferent diffuse interface models for incompressible two-phase flows with different densities. *Mathematical Models and Methods in Applied Sciences*, 22:1150013, 2012.

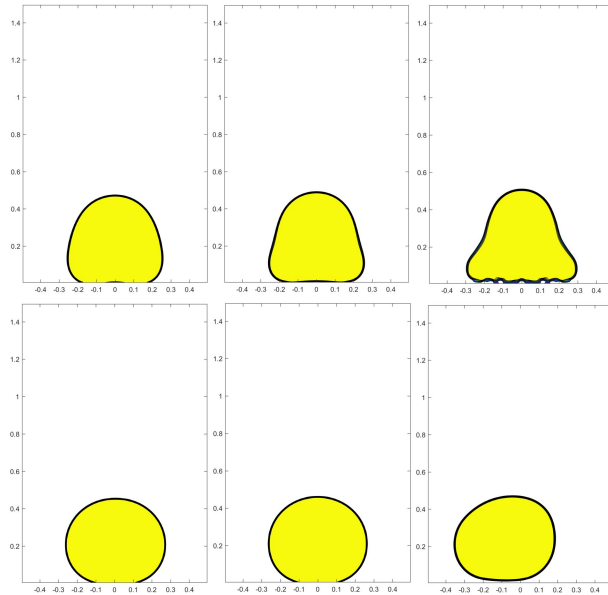


Figure 12: Shapes of the drops with different mobilities. Yellow: water (Phase 1); White: air (Phase 2); From left to right:  $M\lambda = 5 \times 10^{-3}$ ,  $M\lambda = 1 \times 10^{-3}$ , and  $M\lambda = 1 \times 10^{-4}$ . Top:  $t = 0.60$ ; Bottom:  $t = 4.00$ .

- [2] S. Afkhami, S. Zaleski, and M. Bussmann. A mesh-dependent model for applying dynamic contact angles to vof simulations. *Journal of computational physics*, 228(15):5370–5389, 2009.
- [3] S. Aihara, T. Takaki, and N. Takada. Multi-phase-field modeling using a conservative allen-cahn equation for multiphase flow. *Computers & Fluids*, 178:141–151, 2019.
- [4] S.M. Allen and J.W. Cahn. A microscopic theory for antiphase boundary motion and its application to antiphase domain coarsening. *Acta Metallurgica*, 27:1085–1095, 1979.
- [5] D.M. Anderson, G.B. McFadden, and A.A. Wheeler. Diffuse-interface methods in fluid mechanics. *Annu. Rev. Fluid Mech.*, 30:139–165, 1998.
- [6] F. Bai, X. He, X. Yang, R. Zhou, and C. Wang. Three dimensional phase-field investigation of droplet formation in microfluidic flow focusing devices with experimental validation. *Int. J. Multiph. Flow*, 93:130–141, 2017.
- [7] J.U. Brackbill, D.B. Kothe, and C. Zemach. A continuum method for modeling surface tension. *J. Comput. Phys.*, 100:335–354, 1992.
- [8] M. Brassel and E. Bretin. A modified phase field approximation for mean curvature flow with conservation of the volume. *Math Method Appl. Sci.*, 10:1157–1180, 2011.
- [9] J.W. Cahn and J.E. Hilliard. Free energy of a nonuniform system, i interfacial free energy. *J. Chem. Phys.*, 28:258–267, 1958.
- [10] Z. Chai, D. Sun, H. Wang, and B. Shi. A comparative study of local and nonlocal allen-cahn equations with mass conservation. *J. Fluid Mech.*, 122:631–642, 2018.
- [11] P-H Chiu and Y-T Lin. A conservative phase-field method for solving incompressible two-phase flows. *J. Comput. Phys.*, 230:185–204, 2011.
- [12] P.-G. de Gennes, F. Brochard-Wyart, and D. Quere. *Capillarity and Wetting Phenomena*. Springer, 2003.

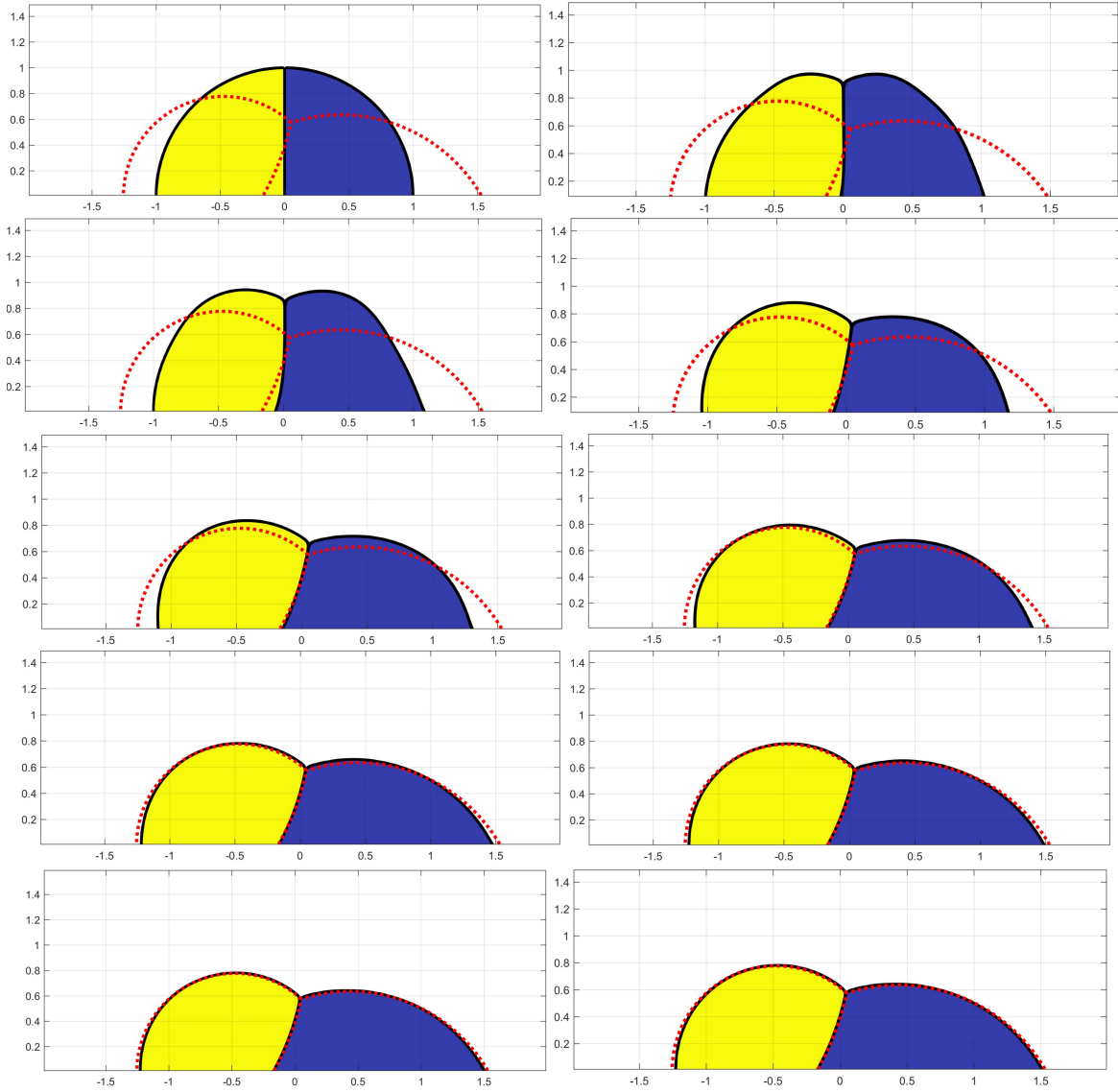


Figure 13: Evolution of the compound drops using Eq.(29) with a stationary bottom wall. Yellow: Phase 1; Blue: Phase 2; White: Phase 3; Red dotted line: exact solution from [65]. From top to bottom and left to right:  $t = 0.0$ ,  $t = 0.2$ ,  $t = 0.4$ ,  $t = 1.0$ ,  $t = 1.4$ ,  $t = 2.0$ ,  $t = 3.0$ ,  $t = 4.0$ ,  $t = 5.0$  and  $t = 6.0$ .

- [13] H. Ding and P.D.M. Spelt. Wetting condition in diffuse interface simulations of contact line motion. *Phys. Rev. E*, 75:046708, 2007.
- [14] S. Dong. On imposing dynamic contact-angle boundary conditions for wall-bounded liquid-gas flows. *Comput. Methods Appl. Mech. Engrg.*, 247-248:179–200, 2012.
- [15] S. Dong. Wall-bounded multiphase flows of nimmiscible incompressible fluids: Consistency and contact-angle boundary condition. *J. Comput. Phys.*, 338:21–67, 2017.
- [16] S. Dong. Multiphase flows of n immiscible incompressible fluids: A reduction-consistent and thermodynamically-consistent formulation and associated algorithm. *J. Comput. Phys.*, 361:1–49, 2018.
- [17] S. Dong and J. Shen. A time-stepping scheme involving constant coefficient matrices for phase-field simulations of two-phase incompressible flows with large density ratios. *J. Comput. Phys.*, 231:5788–5804, 2012.

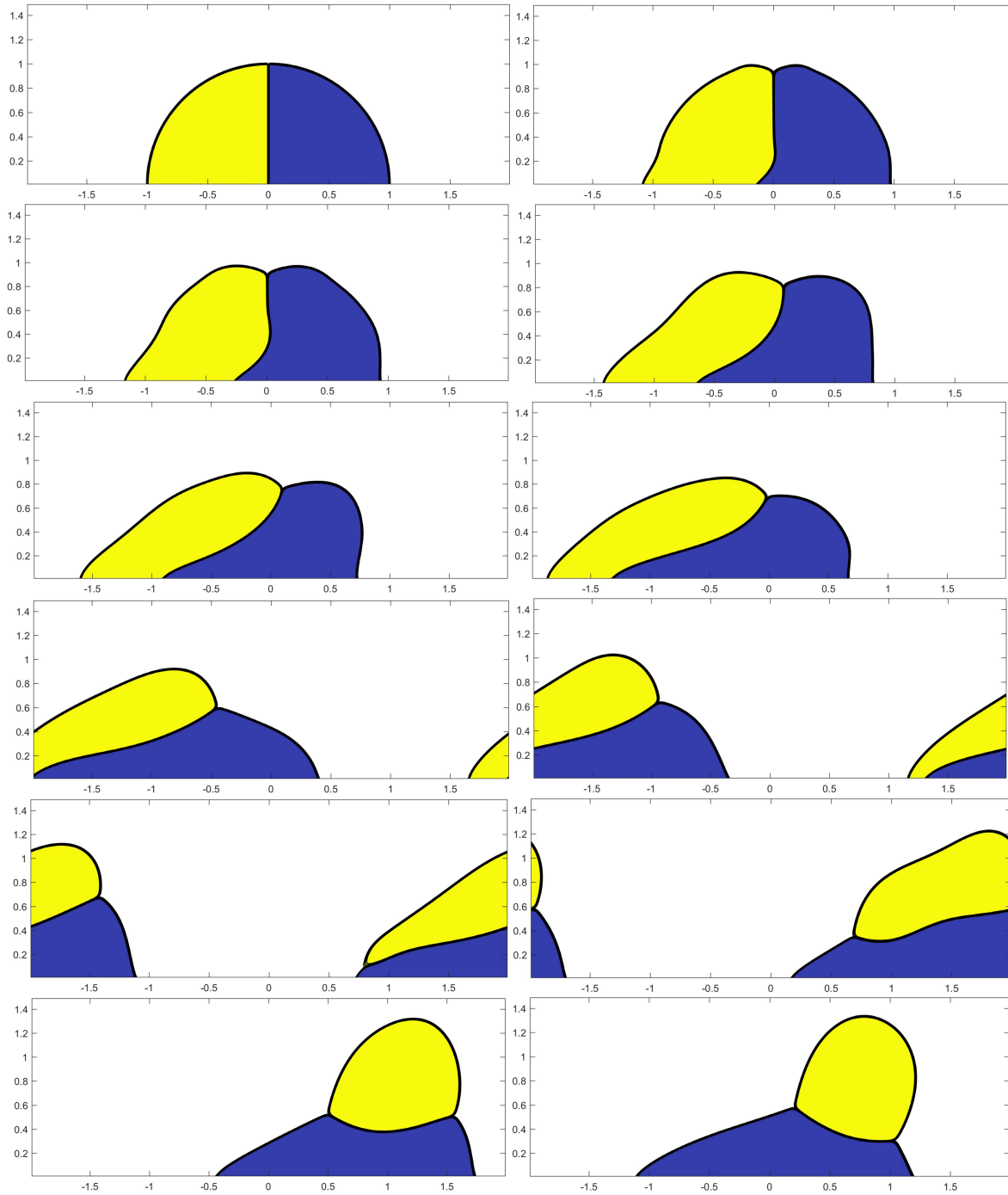


Figure 14: Evolution of the compound drops using Eq.(29) with a translating bottom wall. Yellow: Phase 1; Blue: Phase 2; White: Phase 3. From top to bottom and left to right:  $t = 0.0$ ,  $t = 0.2$ ,  $t = 0.4$ ,  $t = 1.0$ ,  $t = 1.4$ ,  $t = 2.0$ ,  $t = 3.0$ ,  $t = 4.0$ ,  $t = 5.0$ ,  $t = 6.0$ ,  $t = 7.0$ , and  $t = 8.0$ .

[18] J.H. Ferziger and M. Peric. *Computational Methods for Fluid Dynamics*. Springer Berlin / Heidelberg, third, rev. edition. edition, 2001.

[19] C.W. Hirt and B.D. Nichols. Volume of fluid (vof) method for the dynamics of free boundaries. *J. Comput. Phys.*, 39:201–225, 1981.

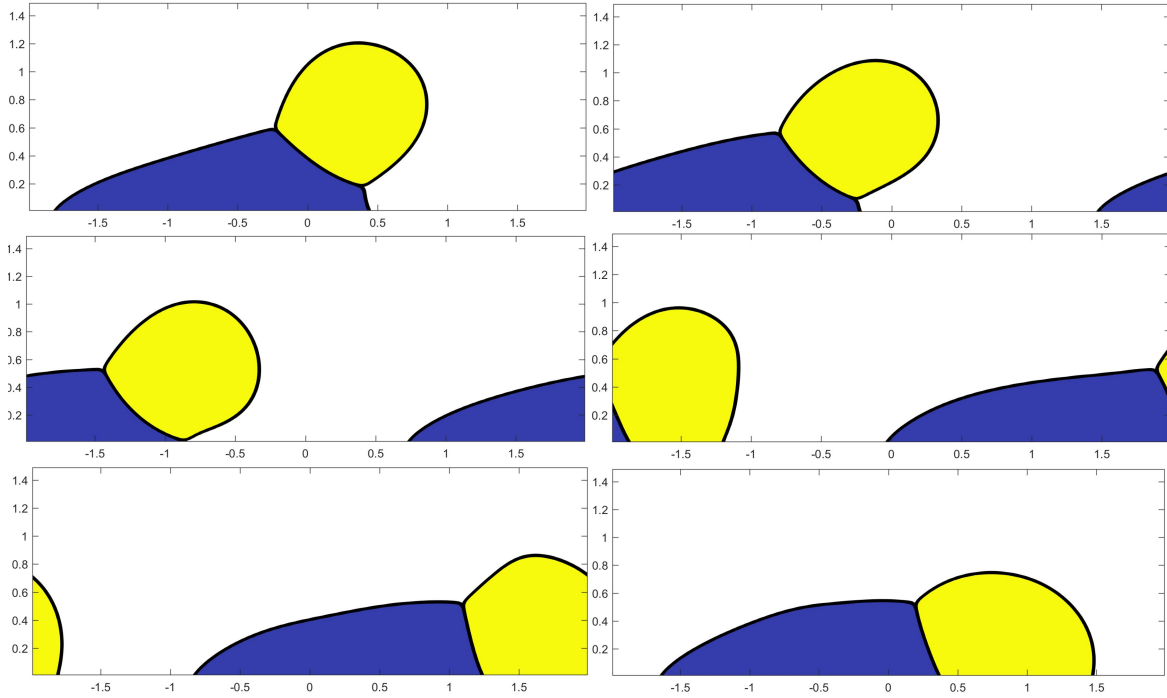


Figure 14 (continued): From top to bottom and left to right:  $t = 9.0$ ,  $t = 10.0$ ,  $t = 11.0$ ,  $t = 12.0$ ,  $t = 13.0$ , and  $t = 14.0$ .

- [20] A.A. Howard and A.M. Tartakovsky. A conservative level set method for n-phase flows with a free-energy-based surface tension model. *Journal of Computational Physics*, page 109955, 2020.
- [21] Y. Hu, D. Li, and Q. He. Generalized conservative phase field model and its lattice boltzmann scheme for multicomponent multiphase flows. *International Journal of Multiphase Flow*, 132:103432, 2020.
- [22] Z. Huang, G. Lin, and A.M. Ardekani. A consistent and conservative phase-field method for multiphase incompressible flows. *arXiv preprint arXiv:2010.01099*, 2020.
- [23] Z. Huang, G. Lin, and A.M. Ardekani. Consistent and conservative scheme for incompressible two-phase flows using the conservative allen-cahn model. *J. Comput. Phys.*, 420:109718, 2020.
- [24] Z. Huang, G. Lin, and A.M. Ardekani. A consistent and conservative volume distribution algorithm and its applications to multiphase flows using phase-field models. *arXiv preprint arXiv:2010.01738*, 2020.
- [25] Z. Huang, G. Lin, and A.M. Ardekani. Consistent, essentially conservative and balanced-force phase-field method to model incompressible two-phase flows. *J. Comput. Phys.*, 406:109192, 2020.
- [26] D. Jacqmin. Calculation of two-phase navier-stokes flows using phase-field modeling. *J. Comput. Phys.*, 155:96–127, 1999.
- [27] D. Jacqmin. Contact-line dynamics of a diffuse fluid interface. *J. Fluid Mech.*, 402:57–88, 2000.
- [28] D. Jeong and J. Kim. Conservative allen-cahn-navier-stokes system for incompressible two-phase fluid flows. *Comput. Fluids*, 156:239–246, 2017.
- [29] G-S Jiang and C-W Shu. Efficient implementation of weighted eno schemes. *J. Comput. Phys.*, 126:202–228, 1996.
- [30] V. Joshi and R.K. Jaiman. An adaptive variational procedure for the conservative and positivity preserving allen-cahn phase-field model. *J. Comput. Phys.*, 336:478–504, 2018.

- [31] V. Joshi and R.K. Jaiman. A positivity preserving and conservative variational scheme for phase-field modeling of two-phase flows. *J. Comput. Phys.*, 360:137–166, 2018.
- [32] J. Kim and H.G. Lee. A new conservative vector-valued allen-cahn equation and its fast numerical method. *Comput. Phys. Commun.*, 221:102–108, 2017.
- [33] J. Kim, S. Lee, and Y. Choi. A conservative allen-cahn equation with a space-time dependent lagrange multiplier. *Int. J. Eng. Sci.*, 84:11–17, 2014.
- [34] U. Lācis, P. Johansson, T. Fullana, B. Hess, G. Amberg, S. Bagheri, and S. Zaleski. Steady moving contact line of water over a no-slip substrate. *The European Physical Journal Special Topics*, 229(10):1897–1921, 2020.
- [35] D. Lee and J. Kim. Comparison study of the conservative allen-cahn and the cahn-hilliard equations. *Math. Comput. Simulation*, 119:35–56, 2016.
- [36] H.G. Lee and J. Kim. Accurate contact angle boundary conditions for the cahn-hilliard equations. *Comput. Fluids*, 44:178–186, 2011.
- [37] J.-C. Loudet, M. Qiu, J. Hemauer, and J.J. Feng. Drag force on a particle straddling a fluid interface: Influence of interfacial deformations. *The European Physical Journal E*, 43(2):1–13, 2020.
- [38] S. Manservigi and R. Scardovelli. A variational approach to the contact angle dynamics of spreading droplets. *Computers & fluids*, 38(2):406–424, 2009.
- [39] S. Mirjalili, C.B. Ivey, and A. Mani. A conservative diffuse interface method for two-phase flows with provable boundedness properties. *J. Comput. Phys.*, 401:109006, 2020.
- [40] S. Mirjalili and A. Mani. Consistent, energy-conserving momentum transport for simulations of two-phase flows using the phase field equations. *Journal of Computational Physics*, 426:109918, 2021.
- [41] M. Muradoglu and S. Tasoglu. A front-tracking method for computational modeling of impact and spreading of viscous droplets on solid walls. *Computers & Fluids*, 39(4):615–625, 2010.
- [42] E. Olsson and G. Kreiss. A conservative level set method for two phase flow. *J. Comput. Phys.*, 210:225–246, 2005.
- [43] E. Olsson, G. Kreiss, and S. Zahedi. A conservative level set method for two phase flow ii. *J. Comput. Phys.*, 225:785–807, 2007.
- [44] S. Osher and A.J. Sethian. Fronts propagating with curvature-dependent speed: Algorithms based on hamilton-jacobi formulations. *J. Comput. Phys.*, 79:12–49, 1988.
- [45] T. Qian, X.P. Wang, and P. Sheng. A variational approach to moving contact line hydrodynamics. *J. Fluid Mech.*, 564:333–360, 2006.
- [46] M. Renardy, Y. Renardy, and J. Li. Numerical simulation of moving contact line problems using a volume-of-fluid method. *Journal of Computational Physics*, 171(1):243–263, 2001.
- [47] Y. Sato and B. Niceno. A new contact line treatment for a conservative level set method. *Journal of computational physics (Print)*, 231(10):3887–3895, 2012.
- [48] R. Scardovelli and S. Zaleski. Direct numerical simulation of free-surface and interfacial flow. *Annu. Rev. Fluid Mech.*, 31:567–603, 1999.
- [49] P. Seppelcher. Moving contact lines in the cahn-hilliard theory. *International journal of engineering science*, 34(9):977–992, 1996.
- [50] J.A. Sethian and P. Smereka. Level set method for fluid interfaces. *Annu. Rev. Fluid Mech.*, 35:341–372, 2003.

- [51] J. Shen, X. Yang, and H. Yu. Efficient energy stable numerical schemes for a phase field moving contact line model. *J. Comput. Phys.*, 284:617–630, 2015.
- [52] L. Shen, H. Huang, P. Lin, Z. Song, and S. Xu. An energy stable c0 finite element scheme for a quasi-incompressible phase-field model of moving contact line with variable density. *Journal of Computational Physics*, 405:109179, 2020.
- [53] Y. Shi and X.-P. Wang. Modeling and simulation of dynamics of three-component flows on solid surface. *Japan Journal of Industrial and Applied Mathematics*, 31(3):611–631, 2014.
- [54] P.D.M. Spelt. A level-set approach for simulations of flows with multiple moving contact lines with hysteresis. *Journal of Computational physics*, 207(2):389–404, 2005.
- [55] Y. Sui, H. Ding, and P.D.M. Spelt. Numerical simulations of flows with moving contact lines. *Annual Review of Fluid Mechanics*, 46:97–119, 2014.
- [56] J. Towns, T. Cockerill, M. Dahan, I. Foster, K. Gaither, A. Grimshaw, V. Hazlewood, S. Lathrop, D. Lifka, G.D. Peterson, R. Roskies, J.R. Scott, and N. Wilkins-Diehr. Xsede: accelerating scientific discovery. *Comput. Sci. Eng.*, 16:62–74, 2014.
- [57] G. Tryggvason, B. Bunner, A. Esmaeeli, D. Juric, N. Al-Rawahi, W. Tauber, J. Han, S. Nas, and Y.J. Jan. A front-tracking method for the computations of multiphase flow. *J. Comput. Phys.*, 169:708–759, 2001.
- [58] S.O. Unverdi and G. Tryggvason. A front-tracking method for viscous, incompressible, multi-fluid flows. *J. Comput. Phys.*, 100:25–37, 1992.
- [59] X. Xu, Y. Di, and H. Yu. Sharp-interface limits of a phase-field model with a generalized navier slip boundary condition for moving contact lines. *Journal of Fluid Mechanics*, 849:805–833, 2018.
- [60] K. Yokoi. Numerical studies of droplet splashing on a dry surface: triggering a splash with the dynamic contact angle. *Soft Matter*, 7(11):5120–5123, 2011.
- [61] P. Yue. Thermodynamically consistent phase-field modelling of contact angle hysteresis. *Journal of Fluid Mechanics*, 899, 2020.
- [62] P. Yue and J.J. Feng. Wall energy relaxation in the cahn–hilliard model for moving contact lines. *Physics of Fluids*, 23(1):012106, 2011.
- [63] P. Yue, C. Zhou, and J.J. Feng. Sharp-interface limit of the cahn–hilliard model for moving contact lines. *J. Fluid Mech.*, 645:279–294, 2010.
- [64] S. Zahedi, K. Gustavsson, and G. Kreiss. A conservative level set method for contact line dynamics. *Journal of Computational Physics*, 228(17):6361–6375, 2009.
- [65] C.Y. Zhang, H. Ding, P. Gao, and Y.L. Wu. Diffuse interface simulation of ternary fluids in contact with solid. *J. Comput. Phys.*, 309:37–51, 2016.
- [66] J. Zhang and P. Yue. A level-set method for moving contact lines with contact angle hysteresis. *Journal of Computational Physics*, 418:109636, 2020.
- [67] Q. Zhang and X.P. Wang. Phase field modeling and simulation of three-phase flow on solid surfaces. *J. Comput. Phys.*, 319:79–107, 2016.
- [68] G. Zhu, J. Kou, J. Yao, A. Li, and S. Sun. A phase-field moving contact line model with soluble surfactants. *J. Comput. Phys.*, 405:109170, 2020.